remote sensing

MDPI

Article

Preliminary Retrieval and Validation of Aerosol Optical Depths from FY-4B Advanced Geostationary Radiation Imager Images

Dong Zhou [1], Qingxin Wang [2], Siwei Li [1,3,4,*] and Jie Yang [1,4]

[1] Hubei Key Laboratory of Quantitative Remote Sensing of Land and Atmosphere, School of Remote Sensing and Information Engineering, Wuhan University, Wuhan 430079, China
[2] College of Geography and Environmental Sciences, Zhejiang Normal University, Jinhua 321004, China
[3] State Key Laboratory of Information Engineering in Surveying, Mapping and Remote Sensing, Wuhan University, Wuhan 430079, China
[4] Hubei Luojia Laboratory, Wuhan University, Wuhan 430079, China
* Correspondence: siwei.li@whu.edu.cn; Tel.: +86-027-68778546

Abstract: Fengyun-4B (FY-4B) is the latest Chinese next-generation geostationary meteorological satellite. The Advanced Geostationary Radiation Imager (AGRI) aboard FY-4B is equipped with 15 spectral bands, from visible to infrared, suitable for aerosol optical depth (AOD) retrieval. In this study, an overland AOD retrieval algorithm was developed for the FY-4B AGRI. Considering the large directional variation in the FY-4B AGRI reflectances, a bidirectional reflectance distribution function (BRDF) database was built, through which to estimate land surface reflectance/albedo. Seasonal aerosol models, based on four geographical regions in China, were developed between 2016 and 2022 using AERONET aerosol products, to improve their applicability to regional distribution differences and seasonal variations in aerosol types. AGRI AODs were retrieved using this new method over China from September 2022 to August 2023 and validated against ground-based measurements. The AGRI, Advanced Himawari Imager (AHI), and Moderate-Resolution Imaging Spectroradiometer (MODIS) official land aerosol products were also evaluated for comparison purposes. The results showed that the AGRI AOD retrievals were highly consistent with the AERONET AOD measurements, with a correlation coefficient (R) of 0.88, root mean square error (RMSE) of 0.14, and proportion that met an expected error (EE) of 65.04%. Intercomparisons between the AGRI AOD and other operational AOD products showed that the AGRI AOD retrievals achieved better performance results than the AGRI, AHI, and MODIS official AOD products. Moreover, the AGRI AOD retrievals showed high spatial integrity and stable performance at different times and regions, as well as under different aerosol loadings and characteristics. These results demonstrate the robustness of the new aerosol retrieval method and the potential of FY-4B AGRI measurements for the monitoring of aerosols with high accuracy and temporal resolutions.

Keywords: FY-4B; AGRI; aerosol optical depth; MODIS

check for updates

Citation: Zhou, D.; Wang, Q.; Li, S.; Yang, J. Preliminary Retrieval and Validation of Aerosol Optical Depths from FY-4B Advanced Geostationary Radiation Imager Images. *Remote Sens.* **2024**, *16*, 372. https://doi.org/10.3390/rs16020372

Academic Editor: Tamas Várnai

Received: 27 November 2023
Revised: 4 January 2024
Accepted: 6 January 2024
Published: 17 January 2024

Copyright: © 2024 by the authors. Licensee MDPI, Basel, Switzerland. This article is an open access article distributed under the terms and conditions of the Creative Commons Attribution (CC BY) license (https://creativecommons.org/licenses/by/4.0/).

1. Introduction

As important components of the ground–atmosphere system, atmospheric aerosols play important roles in global climate change, the environment, and human health. They affect the climate by directly affecting solar radiation and interacting with clouds [1–3]. Increased aerosol loadings can reduce visibility and damage the environment [4]. In addition, studies have shown that exposure to aerosols can increase cardiovascular and respiratory morbidity and mortality [5]. Consequently, the accurate monitoring of aerosols is essential in assessing their impacts on climate change, air quality, and human health.

The aerosol optical depth (AOD), which can quantify the aerosol loadings in the atmosphere, is an essential optical property of aerosols. With the advantage of wide coverage, satellite remote sensing has become an essential means through which to monitor AOD [6]. Polar-orbiting satellite sensors (e.g., Sea-Viewing Wide Field-of-View Sensor (SeaWiFS),

Moderate-Resolution Imaging Spectroradiometer (MODIS), Multi-Angle Imaging Spectroradiometer (MISR), and Visible Infrared Imaging Radiometer Suite (VIIRS)) can provide global observations of aerosol properties [7–10]. However, due to their low temporal resolutions, they cannot capture the daily variations in aerosol characteristics. Geostationary satellite sensors (e.g., Advanced Baseline Imager (ABI), Advanced Himawari Imager (AHI), Geostationary Ocean Color Imager (GOCI), and Advanced Geostationary Radiation Imager (AGRI)) can provide high-temporal-resolution observations, thus providing unique advantages in the continuous, quantitative, and dynamic monitoring of aerosols [11–13].

Many AOD retrieval algorithms have been proposed for different sensors. The most widely known of these algorithms are the dark target (DT) [7,14–16], deep blue (DB) [17,18], and Multi-Angle Implementation of Atmospheric Correction (MAIAC) algorithms [19]. Kaufman et al. (1997) found empirical evidence of a stable surface reflectance relationship between the visible (0.44 and 0.66 μm) and near-infrared (2.1 μm) wavelengths in densely vegetated areas with low reflectance. Based on this principle, they developed the DT algorithm for terrestrial aerosol retrieval. However, the DT algorithm is not applicable for AOD retrieval over bright surfaces [7]. To retrieve the AOD over bright surfaces, such as arid, semi-arid, and urban areas, Hsu et al. (2006) proposed the DB algorithm by precalculating the surface reflectance library [17,18]. Lyapustin et al. (2011) developed the MAIAC algorithm based on time series image analysis to retrieve the AOD over dark and bright surfaces [19]. These algorithms have been applied to produce operational MODIS AOD products.

In terms of geostationary satellite AOD retrieval, the DT algorithm, the minimum reflectance algorithm, and the algorithm based on the surface bidirectional reflectance distribution function (BRDF) data have been widely used [11,12,20–25]. The DT algorithm, developed for dark targets, is not suitable for bright surfaces and shows an overestimation when applied to AHI images [23,24]. The minimum reflectance algorithm assumes that the surface reflectance remains almost constant over a short period, which tends to overestimate the surface reflectance and, therefore, underestimates the AOD because it ignores the presence of background aerosols [20]. Zhang et al. (2019) improved the minimum reflectance algorithm applied to AHI by using ground-based aerosol observations to correct for background aerosols [26]. However, the sparsity of ground-based sites makes it difficult to represent background aerosol properties on a large regional scale. Some AOD retrieval algorithms supported by land BRDF products have been applied to AHI with high accuracy [12,25]. The aforementioned study also showed that the AOD retrieved using the algorithm considering the land BRDF effects had higher accuracy than those based on the DT and minimum reflectance algorithms [27].

The Fengyun 4 (FY-4) series of satellites is the second generation of Chinese geostationary meteorological satellites, operated by the National Satellite Meteorological Center (NSMC) of the China Meteorological Administration (CMA) [28]. The FY-4A is the first experimental satellite of the FY-4 series, launched on 11 December 2016, and it reached its design lifespan by the end of 2021. An AGRI is one of the main sensors carried on the FY-4A, with 14 spectral bands. Some researchers have proposed algorithms for AOD retrieval using the FY-4A AGRI. However, due to the stripe of the blue band, which is the most sensitive band to aerosols, most of the AOD retrieval studies based on the FY-4A AGRI have used other bands. Based on the assumption that the ratios between the surface reflectances of the different channels remain constant over two weeks, Xie et al. (2022) proposed a multi-channel retrieval algorithm, which uses four channels (0.65, 0.83, 1.61, and 2.25 μm) of AGRI and MODIS AOD data, and successfully applied them to FY-4A AOD retrieval in South Asia [29]. Jiang et al. (2022) established a monthly average surface reflectance ratio library of 0.65 μm/2.22 μm using MODIS AOD data and proposed a band ratio library (BRL) algorithm for the retrieval of FY-4A AGRI AOD data over land [30].

As the first operational satellite of the FY-4 series, the FY-4B was launched on 3 June 2021; it carries four sensors to detect the atmospheric and space environments. The AGRI onboard the FY-4B has 15 spectral bands and is more stable compared to the FY-4A/AGRI,

with no obvious stripe in the blue band. Due to its high temporal resolution of 15 min and complete coverage of China, the FY-4B AGRI is of great importance for aerosol research in China. However, the FY-4B official land aerosol product (FY4B_LDA), provided by the CMA, is based on the DT algorithm, which is not applicable to bright surfaces. In addition, there are few studies on AOD retrieval for the FY-4B AGRI. Therefore, in order to better utilize FY-4B data for aerosol monitoring, it is essential to develop an accurate aerosol retrieval algorithm based on FY-4B AGRI observations.

In this study, we developed a high-precision algorithm with which to retrieve AOD data from FY-4B AGRI observations. A monthly BRDF database was built to determine the land surface reflectance/albedo, to reduce the errors caused by the surface Lambertian hypothesis. Considering the regional and seasonal differences of aerosols, 16 aerosol models for different seasons and regions were established based on ground-based aerosol products from 2016 to 2022. The AGRI AOD was retrieved using the proposed method, over land in China, and validated based on AERONET AOD measurements, as well as being compared with the FY4B_LDA AOD, AHI AOD, and MODIS AOD products. The study area and data source are introduced in Section 2. Section 3 describes the methodology. The results and validation are discussed in Section 4. Section 5 summarizes the conclusions.

2. Data Source and Study Area

2.1. FY-4B AGRI Data

The FY-4B geostationary meteorological satellite was launched from the Xichang Satellite Launch Center on 3 June 2021 and was located above the equator at 133°E. Since 1 June 2022, observational data and application services from the FY-4B have been available for users worldwide. The AGRI is one of the main payloads onboard the FY-4B, which has 15 spectral bands from 0.47 to 13.3 μm, with spatial resolutions from 500 m to 4 km. The detailed characteristics of the spectral bands of the AGRI are shown in Table 1. The FY-4B AGRI can perform a full-disk observation every 15 minutes and complete 95 full-disk observations per day normally. The characteristics of the band setting and high-frequency observations of the AGRI make it favorable for the monitoring of the diurnal variation in the AOD in China. In this study, the FY-4B AGRI L1 radiance data and the geometry positioning (GEO) data with a spatial resolution of 4 km from September 2022 to August 2023 were collected from the CMA website (http://satellite.nsmc.org.cn/portalsite/data/Satellite.aspx, accessed on 5 January 2024). In addition, the official L2 land aerosol (FY4B_LDA) product for the same period was also downloaded for comparison. The FY4B_LDA AOD product with all data quality flags (DQF) was used in the validation.

Table 1. Bands and key parameters of the FY-4B AGRI.

Band	Center Wavelength (μm)	Band Width (μm)	Spatial Resolution (km)
1	0.47	0.45–0.49	1
2	0.65	0.55–0.75	0.5
3	0.825	0.75–0.90	1
4	1.379	1.371–1.386	2
5	1.61	1.58–1.64	2
6	2.225	2.10–2.35	2
7	3.75	3.50–4.00 (high)	2
8	3.75	3.50–4.00 (low)	4
9	6.25	5.80–6.70	4
10	6.95	6.75–7.15	4
11	7.42	7.24–7.60	4
12	8.55	8.30–8.80	4
13	10.80	10.30–11.30	4
14	12.00	11.50–12.50	4
15	13.30	13.00–13.60	4

2.2. MODIS Data

The MODIS is a crucial sensor onboard the Terra and Aqua satellites, which provides observations in 36 spectral bands from visible to thermal infrared (0.4 to 14.4 μm). With the advantages of a wide range of wavelengths, high spatial resolution, and short revisit periods, MODIS observations have been widely used for global-scale surface and atmospheric studies.

The MODIS AOD is the most popular satellite aerosol product currently available. The MxD04_L2 products (representing both MOD04 and MYD04 products) are the standard MODIS aerosol products, containing AOD datasets retrieved by two different algorithms (DT and DB), with a spatial resolution of 10 km [14,17,18]. In this study, the Collection 6.1 aerosol products (MxD04_L2) with all quality flags from September 2022 to August 2023, provided by the National Aeronautics and Space Administration (NASA), were collected for comparison with the AOD retrieved from the FY-4B AGRI observations.

The MCD19A3 is an L3 BRDF parameter product retrieved by the MAIAC algorithm [19,31], which provides three coefficients (weights) of the Ross-thick/Li-sparse (RTLS) BRDF model (Kiso: isotropic kernel; Kvol: volumetric kernel; Kgeo: geometric kernel) for bands 1–8. The MCD19A3 product has a spatio-temporal resolution of 1 km in 8 days, enabling full surface coverage [31]. The MCD19A3 data were used as prior knowledge of surface reflectance to support the AGRI AOD retrieval in this study.

2.3. Himawari-8/9 AHI Data

Himawari-8/9 are Japan's new-generation geostationary orbiting meteorological satellites, launched on 7 October 2014 and 2 November 2016, respectively. They carry the AHI, which has 16 spectral bands similar to the MODIS [32]. The L2 aerosol product, provided by the Japan Aerospace Exploration Agency (JAXA), has a spatial resolution of 5 km and a temporal resolution of 10 min. The JAXA AOD retrieval algorithm estimates land surface reflectances based on a pre-calculated surface reflectance database, which is similar to the DB algorithm. Due to the advantages of a high temporal resolution and wide observation range, the official JAXA aerosol products have been extensively utilized in aerosol studies in China. The official Level 2 aerosol products from September 2022 to August 2023 were downloaded from the JAXA in this study. Moreover, the AHI AOD product with all quality assessment flags (QA_flag) was used for comparison.

2.4. AERONET Data

The Aerosol Robotic Network (AERONET) is a ground-based remote sensing aerosol network jointly established by NASA (located in the United States) and PHOTONS (PHOtométrie pour le Traitement Opérationnel de Normalisation Satellitaire; located in Lille, France) to measure aerosol optical properties and obtain other atmospheric information [33]. AERONET can provide accurate AOD data with uncertainty of about 0.01, which is commonly used as the true value for satellite AOD product validation [34,35]. The AERONET sites also provide other aerosol property parameters at different wavelengths, including the Ångström exponent (AE), single scattering albedo (SSA), refractive index, asymmetry factor, and aerosol size distribution, etc., which have been widely used to build aerosol models to improve the accuracy of AOD retrievals from satellite observations [36–39].

The Version 3 AOD data are provided for three quality levels: Level 1.0 (unscreened), Level 1.5 (cloud-screened and quality-controlled), and Level 2.0 (quality-assured). Level 1.5 products are available almost in real time, whereas Level 2.0 products may present a delay of more than 12 months [40]. Within the timeframe of this study (from September 2022 to August 2023), the Level 2.0 products had a significant amount of data missing at the sites within the study area. In contrast, the Level 1.5 products had more available data. Therefore, the Level 1.5 products were used to validate the AOD retrievals from the AGRI in this study. A summary of the AERONET sites used for AOD validation is shown in Table 2.

Table 2. Summary of the AERONET sites used for AOD validation in this study.

Site Name	Latitude (°N)	Longitude (°E)	Altitude (m)
AOE_Baotou	40.852	109.629	1314
Beijing	39.977	116.381	92
Beijing-CAMS	39.933	116.317	106
Beijing_PKU	39.992	116.310	53
Beijing_RADI	40.005	116.379	59
Chen-Kung_Univ	22.993	120.205	50
Douliu	23.712	120.545	60
EPA-NCU	24.968	121.185	144
Hong_Kong_PolyU	22.303	114.180	30
Kaohsiung	22.676	120.292	15
Lulin	23.469	120.874	2868
TASA_Taiwan	24.784	121.001	99
XiangHe	39.754	116.962	36

In addition, to build aerosol models in China, we also downloaded the Level 2.0 aerosol products (for SSA, phase function, volume distribution, complex refraction index, and other parameters) from 2016 to 2022. The Level 1.5 aerosol products were used as a supplement when Level 2.0 data were missing at some sites. The stations used for aerosol model building in this study are shown in Figure 1.

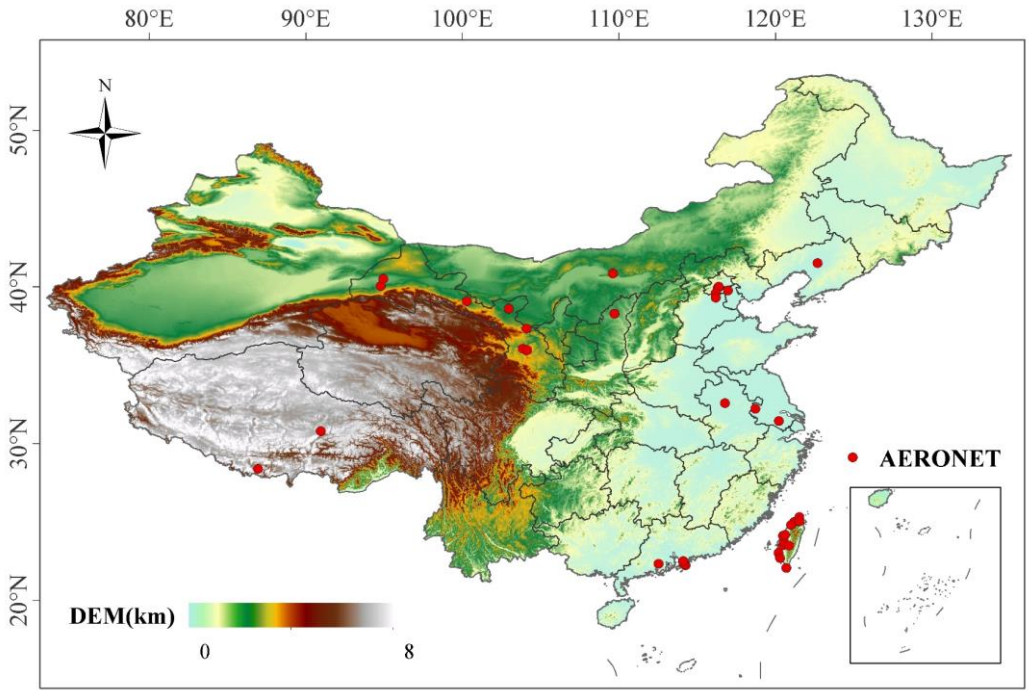


Figure 1. Study area and the distribution of the AERONET sites for aerosol model building.

2.5. Study Area

China's land area is located in Eastern Asia, along the western coast of the Pacific Ocean, spanning latitudes and longitudes ranging from 73°E to 135°E and 18°N to 54°N, as shown in Figure 1. The complex topography, diverse surface and climate types, and differential distribution of cities and populations in China result in the diversity of aerosol sources and properties. The frequent occurrence of pollution incidents has drawn attention to aerosol research in the region.

3. Method

The determination of surface reflectance and aerosol models is a crucial factor in AOD retrieval because the signals received by satellite sensors are composed of contributions from both the atmosphere and the surface. Cloud, ice/snow, and inland water pixels that are not suitable for AOD retrieval were masked before retrieval based on previous research [18,41,42]. Aerosol modeling, surface reflectance determination, and retrieval methods are described in this section. The flowchart of the AOD retrieval algorithm in this study is shown in Figure 2.

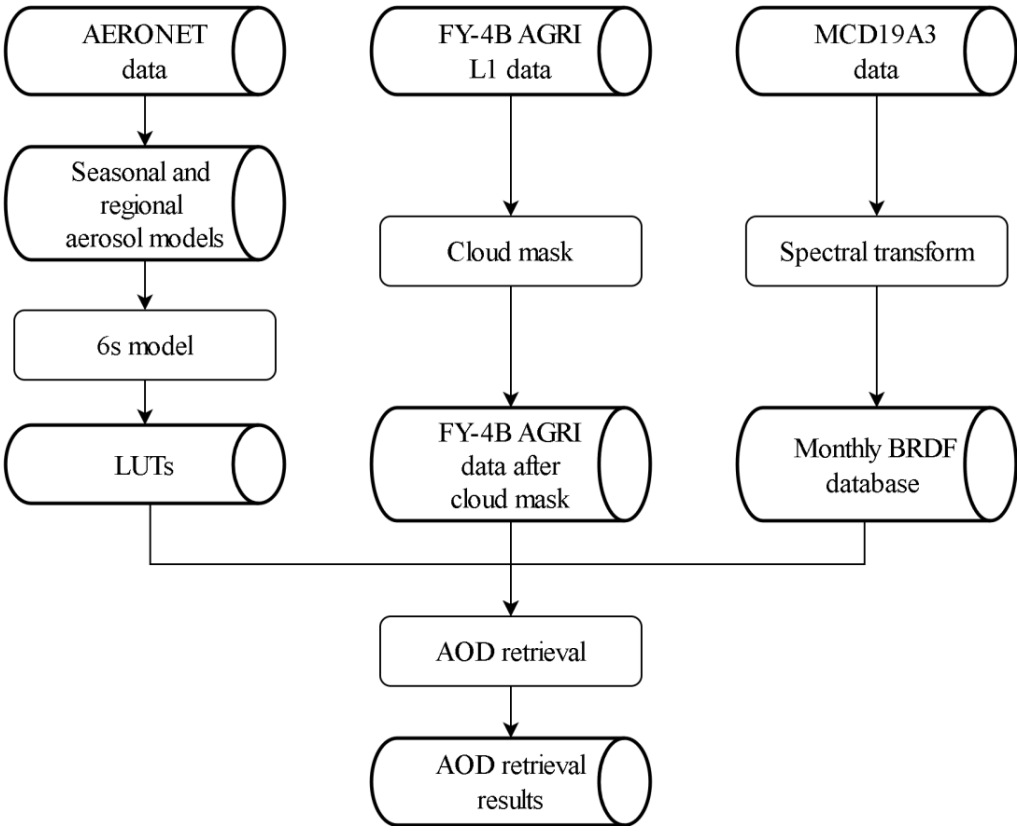


Figure 2. Flowchart of the FY-4B AGRI AOD retrieval algorithm.

3.1. Aerosol Model

The physical and optical properties of different aerosol types vary significantly, causing different atmospheric scattering effects. An unsuitable assumption of the aerosol model will lead to large uncertainties in AOD retrieval. Therefore, an accurate aerosol model assumption is one of the key factors for AOD retrieval from satellite measurements.

In general, aerosol models used for AOD retrieval are mainly obtained from existing databases or built based on AERONET data. The available dataset contains typical aerosol models, such as the continental model, which has been widely used for AOD retrieval in China. However, the aerosol types in China have changed in recent years, and the existing aerosol models do not accurately represent the current aerosol properties. Therefore, it is necessary to build new aerosol models in China. In addition, studies have shown seasonal and regional differences in aerosol types [37,43–46]. For example, the aerosol properties vary significantly on either side of the Hu line. Natural aerosols are predominant in the west of the Hu line, while anthropogenic aerosols dominate in the east [44,47]. There are also differences in aerosol properties between the northern and southern regions of China, with higher absorption and larger particle sizes in the north and stronger scattering and smaller particle sizes in the south [48,49]. Thus, more refined aerosol models depending

on the regions and seasons were constructed based on the AERONET data in this study to better represent the actual aerosols.

There are four geographical regions in China: the Qinghai–Tibet region (QTR), northwest region (NWR), south region (SR), and north region (NR) (as shown in Figure 3). Each region differs in population, topography, climate, precipitation, and humidity. These variations are accompanied by differences in urban/industrial activity, agricultural biomass burning, etc., which cause differences in the sources of aerosols [50,51]. Due to the unique topography (with an average altitude exceeding 4000 m) and sparse population, the characteristics and concentrations of aerosols in the QTR are different from those in other regions. Northwest China, a typical arid and semi-arid region with a predominantly temperate continental climate, is a major source area for dust in China, characterized by a high frequency of dust aerosols. Dust aerosols from the northwest can be carried to the Qinghai–Tibet Plateau and the northern region, affecting the local aerosol properties [52,53]. The northern and southern regions are delineated by the Qinling–Huaihe line. The northern region experiences a predominantly temperate monsoon climate, while the southern region has a primarily subtropical monsoon climate, characterized by higher humidity and forest cover. These differences may affect the aerosol concentrations and properties [51]. In addition, the north–south boundary line is similar to the north–south heating line, which is the dividing line of winter heating in China. There is wintertime warming provided in the northern part of this line, which may result in differences in aerosol properties during the winter [44]. Considering the evolving aerosol types in China in recent years and the characteristics of regional and seasonal differences, it is necessary to establish aerosol models tailored to the different seasons and regions. In addition, to improve the efficiency of the algorithm, this study established candidate aerosol models for each region and season by averaging the parameters from the AERONET data from 2016 to 2022.

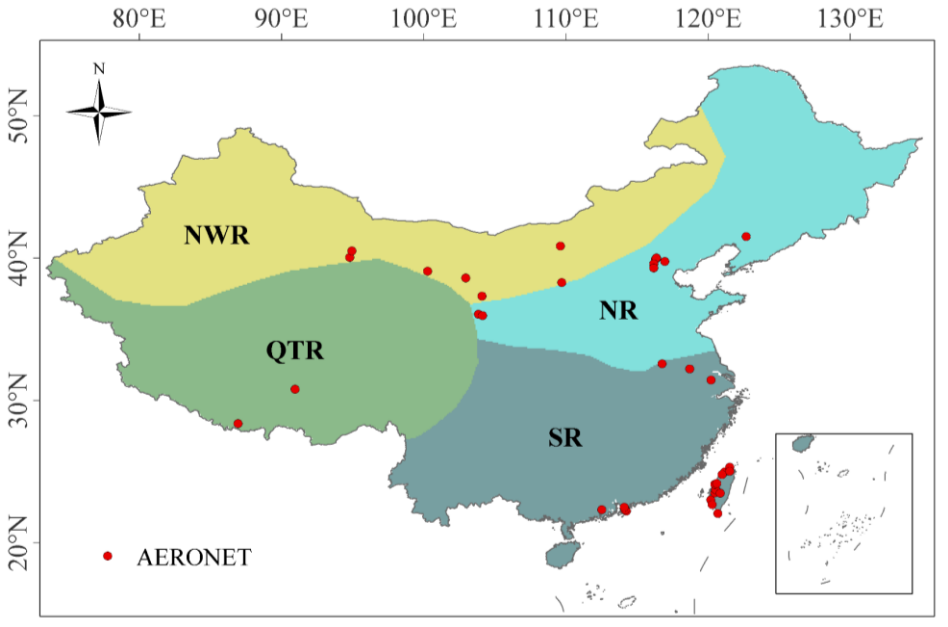


Figure 3. Four geographical regions of China.

Figure 4 shows the mean values of the optical parameters and size distributions for each aerosol model, and Table 3 shows some detailed parameters of the aerosol models. In the QTR, except for spring, the size distributions of aerosol models for all seasons were relatively similar, with a bimodal distribution dominated by coarse particles. The SSA values of the four models exhibited a consistent wavelength dependence that decreased with an increasing wavelength, with the lowest values observed in winter and the highest in spring. The AE values of aerosol models in the QTR ranged from 0.95 to 1.21, with the lowest values observed in summer. NWR-spring was dominated by coarse particles,

with a peak in SSA at the wavelength of 675 nm. The SSA values of the remaining models in the NWR decreased with an increasing wavelength. No obvious dominant peak in size distribution was found in NWR-summer and NWR-autumn, while NWR-winter was dominated by fine particles. The AEs of aerosol models in NWR ranged from 0.6 to 1.3, with the lowest in spring, indicating the largest aerosol particles. All aerosol models in the NR showed bimodal distributions, with coarse particles dominating in spring, while no obvious dominant peak in size distribution was observed in the other seasons. The SSA values of aerosol models in the NR showed a small peak at the wavelength of around 675 nm, except for NR-summer. The seasonal characteristics of the AE in the NR (ranging from 1.05 to 1.28) were similar to those in the NWR, with the lowest in spring. The four aerosol models in the SR showed bimodal distributions dominated by fine particles. The SSA decreased with an increasing wavelength for all SR aerosol models, except in winter, when a local peak occurred at 675 nm. The AE values in the SR ranged from 1.25 to 1.47, with a peak occurring in summer.

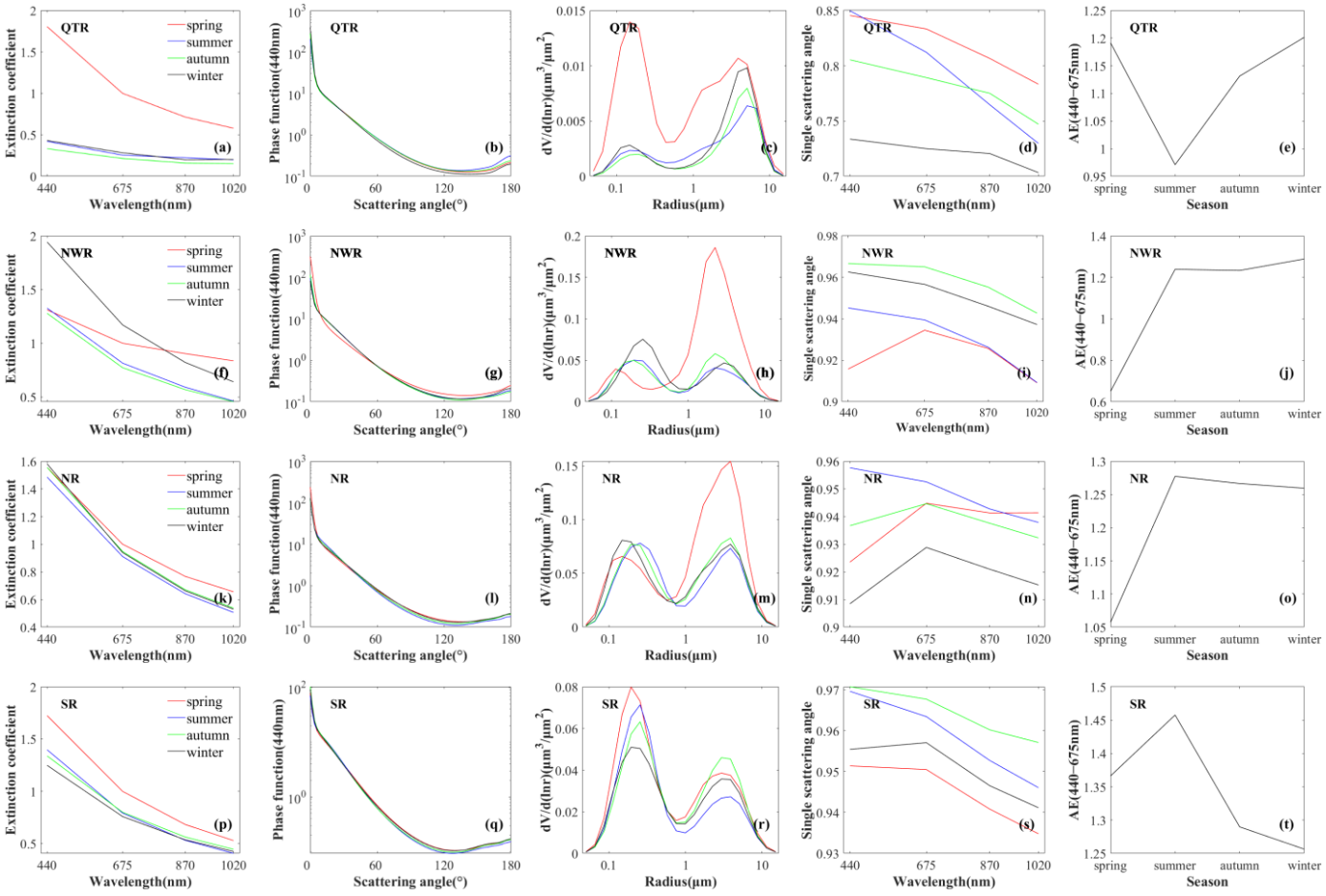


Figure 4. The aerosol optical models of average results for four seasons in QTR, NWR, NR, and SR. (**a**,**f**,**k**,**p**) are extinction coefficients; (**b**,**g**,**l**,**q**) are phase functions at 440 nm; (**c**,**h**,**m**,**r**) are size distributions; (**d**,**i**,**n**,**s**) are single scattering albedo; (**e**,**j**,**o**,**t**) are AE indices at 440–675 nm.

Table 3. Some detailed parameters of the aerosol models.

Aerosol Models		SSA (440/675/870/1020 nm)	REER [1] (440/675/870/1020 nm)	REEI [1] (440/675/870/1020 nm)	VC-F [2] ($\mu m^3/\mu m^2$)	Std-F [2]	VC-C [2] ($\mu m^3/\mu m^2$)	Std-C [2]
QTR	spring	0.85/0.83/0.81/0.78	1.55/1.55/1.55/1.54	0.028/0.024/0.026/0.029	0.02	0.48	0.02	0.73
	summer	0.85/0.81/0.76/0.73	1.56/1.56/1.55/1.55	0.027/0.030/0.037/0.044	0.01	0.52	0.01	0.73
	autumn	0.81/0.79/0.78/0.75	1.56/1.56/1.56/1.56	0.042/0.037/0.034/0.037	0.01	0.52	0.01	0.60
	winter	0.73/0.73/0.72/0.70	1.56/1.56/1.56/1.56	0.066/0.051/0.043/0.043	0.01	0.49	0.01	0.59
NWR	spring	0.92/0.93/0.93/0.91	1.51/1.52/1.53/1.53	0.006/0.005/0.006/0.008	0.05	0.55	0.27	0.62
	summer	0.95/0.94/0.93/0.91	1.46/1.47/1.49/1.48	0.008/0.008/0.009/0.010	0.08	0.51	0.07	0.60
	autumn	0.97/0.97/0.96/0.94	1.45/1.46/1.47/1.46	0.004/0.003/0.004/0.005	0.07	0.50	0.08	0.58
	winter	0.96/0.96/0.95/0.94	1.49/1.48/1.49/1.48	0.005/0.004/0.005/0.006	0.10	0.51	0.07	0.59
NR	spring	0.92/0.94/0.94/0.94	1.50/1.51/1.52/1.51	0.007/0.004/0.004/0.004	0.11	0.49	0.25	0.62
	summer	0.96/0.95/0.94/0.94	1.45/1.45/1.45/1.45	0.005/0.005/0.005/0.005	0.12	0.50	0.11	0.59
	autumn	0.94/0.94/0.94/0.93	1.49/1.49/1.49/1.48	0.008/0.005/0.006/0.006	0.12	0.50	0.13	0.61
	winter	0.91/0.93/0.92/0.92	1.49/1.50/1.51/1.50	0.012/0.007/0.007/0.008	0.12	0.52	0.13	0.63
SR	spring	0.95/0.95/0.94/0.93	1.43/1.44/1.44/1.44	0.006/0.006/0.006/0.006	0.11	0.50	0.07	0.63
	summer	0.97/0.96/0.95/0.95	1.39/1.40/1.40/1.40	0.004/0.004/0.004/0.005	0.10	0.48	0.05	0.60
	autumn	0.97/0.97/0.96/0.96	1.41/1.41/1.41/1.41	0.003/0.003/0.004/0.004	0.09	0.50	007	0.60
	winter	0.96/0.96/0.95/0.94	1.43/1.43/1.44/1.43	0.005/0.005/0.005/0.005	0.08	0.53	0.06	0.61

[1] REER and REEI are the real and imaginary parts of the complex refractive index. [2] VC and Std are the volume concentration and standard deviation of the effective radius. F refers to fine. C refers to coarse.

3.2. Determination of Surface Reflectance

The accurate estimation of surface reflectance is important for AOD retrieval from satellite observations, especially when the aerosol loading is low (as the satellite observation signals are mainly derived from surface reflectance). Some methods have been proposed for the determination of surface reflectance, such as the DT and DB algorithms. These methods have improved the accuracy of AOD retrieval from satellite observations, but further improvements are still necessary. The DT algorithm developed for dense vegetation areas is not applicable to bright surfaces, while the DB and minimum reflectance algorithms are not suitable for areas dominated by absorptive aerosols [54]. In addition, these algorithms are based on a Lambertian surface assumption and ignore the coupling of the surface and atmosphere, leading to potential errors in AOD retrieval. Studies have demonstrated the robustness of using MODIS BRDF products to build a BRDF parameter library for AOD retrieval [12,25,42]. The MCD19A3 is a MODIS BRDF product retrieved by the MAIAC algorithm, which provides BRDF model parameters. Therefore, we constructed a monthly BRDF parameter database in the blue band to calculate the surface reflectance/albedo of the FY-4B AGRI using MCD19A3 data under the assumption that the shape and the albedo amplitude of BRDF remain constant over a month, following the method of Wang et al. (2020; 2023) [25,42]. We used a minimum standard deviation method to determine the BRDF shape parameters by taking the mean of the four images with the smallest standard deviation over a month as the final value for each pixel. The differences in spectral response functions, wavelengths, and viewing angles between the MODIS and AGRI resulted in differences in LSR values at the same pixel for the same band (Figure 5). Consequently, it was necessary to establish a spectral transformation model between the MODIS and AGRI LSRs for the blue band. The spectral curves of different features were collected from the United States Geological Survey (USGS) spectral library, and LSR values at the blue band were calculated for the MODIS and AGRI, respectively [25]. Based on the assumption that the LSR between the AGRI and MODIS is linear, the spectral transformation model between the MODIS and AGRI can be calculated (Figure 5b).

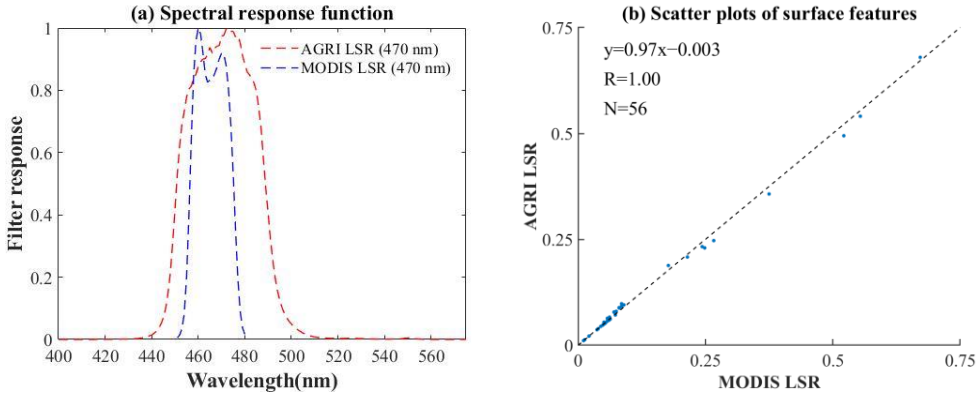


Figure 5. (**a**) Spectral response function between the MODIS and AGRI blue wavebands. (**b**) Scatter plots of different surface features of the MODIS and AGRI. The black line is the 1:1 line.

3.3. Look-Up Table Building

To improve the retrieval efficiency, we pre-calculated look-up tables (LUTs) for each aerosol model using the 6SV2.1 model in this study. These LUTs included different solar zenith angles, satellite zenith angles, relative azimuth angles, AODs, aerosol models, surface elevations, BRDF parameters, and calculated TOA reflectances. In order to avoid the drawback that Mie scattering is not applicable to non-spherical aerosol particles, we established aerosol models by directly modifying the aerosol optical parameters (e.g., SSA, phase function) in the 6S model using the statistical results from the AERONET data, instead of using the interface for Mie scattering calculation in the 6S model. The AOD values at 550 nm were calculated by comparing the apparent reflectance from satellite observations with the apparent reflectance simulated by the radiative transfer model in the blue band. The details of the LUT settings are shown in Table 4.

Table 4. Details of the setting of LUTs.

Variable	Value
Solar zenith angle (°)	0, 12, 24, 36, 48, 60, 72
Viewing zenith angle (°)	0, 13, 26, 39, 52, 65, 78
Relative azimuth angle (°)	0, 30, 60, 90, 120, 150, 180
Aerosol type	QTR, NWR, NR, SR for different seasons
AOD at 550 nm	0.01, 0.05, 0.1, 0.2, 0.3, 0.4, 0.5, 0.7, 1.0, 1.5, 2.0, 2.5, 3.5
Elevation (km)	NWR, NR, SR: 0, 0.5, 1.5, 5
Wavelength (μm)	QTR: 1, 4, 7 AGRI 0.47
BRDF_Kiso	0.001, 0.02, 0.04, 0.06, 0.08, 0.10, 0.15, 0.20, 0.25, 0.35
BRDF_Kgeo	0, 0.02, 0.04, 0.06, 0.08
BRDF_Kvol	0, 0.02, 0.04, 0.06, 0.08

4. Results and Validation

4.1. AOD Validation Using AERONET Data

The 10-km AOD values were retrieved from the FY-4B AGRI observations and validated against the AERONET AOD measurements in China from September 2022 to August 2023. The FY4B_LDA AOD, MODIS (DT and DB) AOD, and AHI AOD products were also validated using the ground-based AOD for comparison purposes. The AOD retrievals from different satellites and ground-based measurements should be matched in terms of the spectral, temporal, and spatial domains first. The AERONET and AHI AOD values need to be converted to 550 nm to match the wavelength of the AGRI and MODIS AOD products. For the AERONET AOD, the AOD spectra conversion was performed using the following equation:

$$\tau(\lambda) = \beta\lambda^{-\alpha}, \quad (1)$$

where α is the Ångström exponent (AE), λ is the wavelength, $\tau(\lambda)$ is the AOD value at the wavelength of λ, and β represents the turbidity coefficient. Based on this equation, the AOD values at 550 nm can be calculated using the 500 nm and 675 nm AOD values provided by the AERONET measurements.

For the AHI AOD, a simple linear relationship was used to convert the 500 nm AOD to the 550 nm AOD [25], which can be expressed as follows:

$$\mathrm{AOD}_{550} = 0.883 \times \mathrm{AOD}_{500} + 0.02, \tag{2}$$

where AOD_{500} and AOD_{550} are the AOD values at wavelengths of 500 nm and 550 nm, respectively.

Regarding spatial and temporal matching, the satellite AOD retrievals were averaged within a 30 km × 30 km pixel grid centered on the ground-based site, while the ground-based AOD values were averaged within 30 min of the satellite overpass time [39,55].

The ground-based and satellite AOD matchups were linearly fitted based on the least squares principle. The correlation coefficient (R), root mean square error (RMSE), mean absolute error (MAE), mean relative error (MRE), expected error (EE), and relative mean deviation (RMB) were calculated to evaluate the accuracy of the satellite AOD retrievals. These statistical parameters were defined as follows [56,57]:

$$\mathrm{R} = \frac{\sum_{i=1}^{n}\left(AOD_{(satellite)_i} - \overline{AOD_{(satellite)}}\right)\left(AOD_{(AERONET)_i} - \overline{AOD_{(AERONET)}}\right)}{\sqrt{\sum_{i=1}^{n}\left(AOD_{(satellite)_i} - \overline{AOD_{(satellite)}}\right)^2}\sqrt{\sum_{i=1}^{n}\left(AOD_{(AERONET)_i} - \overline{AOD_{(AERONET)}}\right)^2}} \tag{3}$$

$$\mathrm{RMSE} = \sqrt{\frac{1}{n}\sum_{i=1}^{n}\left(AOD_{(satellite)_i} - AOD_{(AERONET)_i}\right)^2} \tag{4}$$

$$\mathrm{MAE} = \frac{1}{n}\sum_{i=1}^{n}\left|AOD_{(satellite)_i} - AOD_{(AERONET)_i}\right| \tag{5}$$

$$\mathrm{MRE} = \frac{1}{n}\sum_{i=1}^{n}\left(\frac{AOD_{(satellite)_i} - AOD_{(AERONET)_i}}{AOD_{(AERONET)_i}}\right) \tag{6}$$

$$\mathrm{EE} = \pm(0.05 + 0.2 \times AOD_{AERONET}) \tag{7}$$

$$\mathrm{RMB} = \overline{AOD_{satellite}} / \overline{AOD_{AERONET}} \tag{8}$$

where $AOD_{satellite}$ and $AOD_{AERONET}$ are the AOD values from the satellite and AERONET products, respectively.

4.1.1. Overall Validation

The overall validation results (Figure 6) showed that the AGRI AOD retrievals agreed well with the ground-based AOD, with a correlation coefficient of 0.88, which was higher than that of the other AOD products. MODIS products also were highly consistent with the ground-based AOD, with R exceeding 0.85. However, the correlation coefficients of the FY4B_LDA and AHI AOD products were only 0.65 and 0.77, showing low consistency with the ground-based AOD. The AGRI AOD retrievals also showed a lower RMSE (0.14), MAE (0.1), and MRE (0.57) than other AOD products, indicating that the deviation between the AGRI AOD retrievals and ground-based AOD was smaller. In addition, the AGRI AOD retrievals exhibited a higher proportion of AOD matchups within the expected error envelopes (65.04%) compared to the other four products. The RMB of the AGRI retrievals was 0.94, and 20.35% of the samples were below the EE line, indicating an underestimation of the algorithm. The RMB values of the other four AOD products all exceeded 1.1, with more than 28% of the samples falling above the EE line, showing overestimation. In particular, the FY4B_LDA AOD product exhibited a strong overestimation, with an RMB of 1.97 and a proportion that met the expected error (EE) of 57.13%. However, due to the stricter cloud detection method that we used to ensure data quality, fewer valid results

were obtained compared to the FY4B_LDA and AHI AOD products, resulting in fewer points matched (6931). In the future, we will improve the cloud detection algorithm to obtain as many valid results as possible under the premise of ensuring the results' quality.

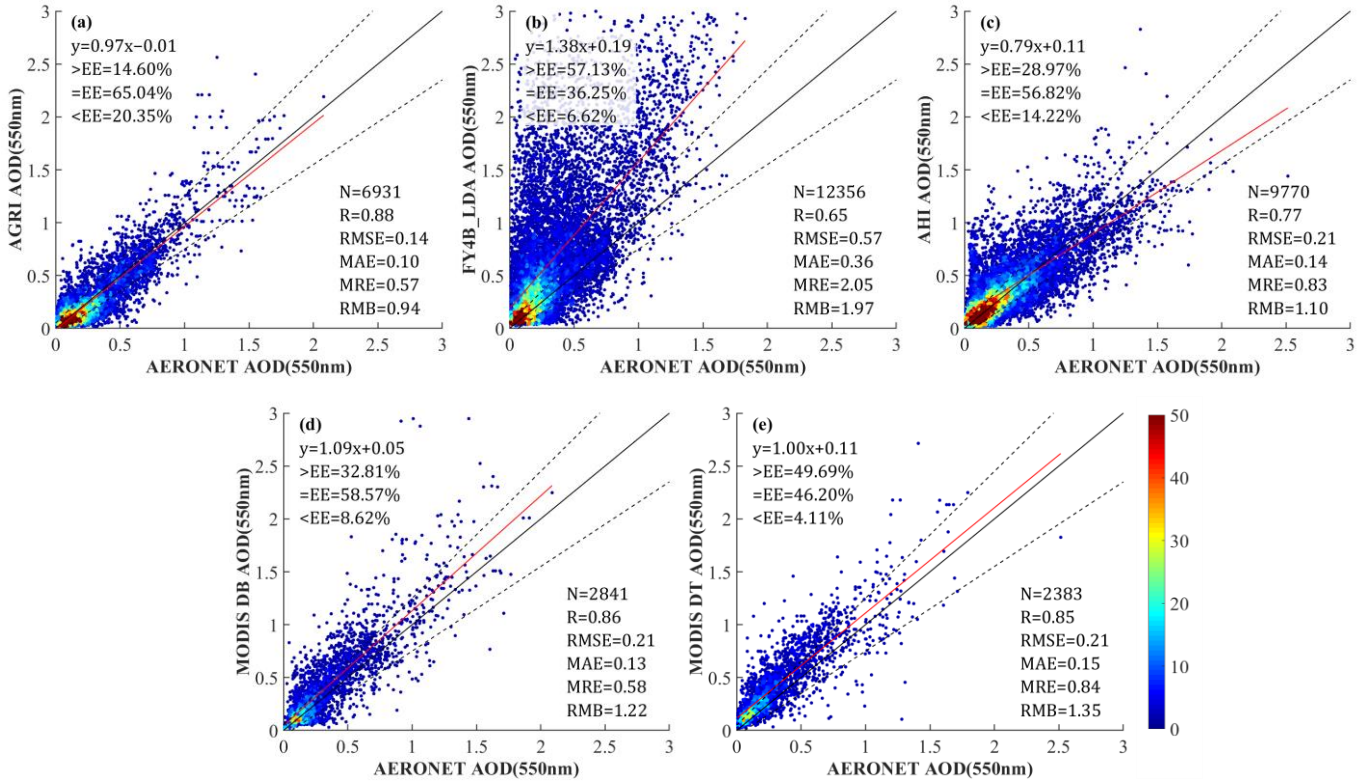


Figure 6. Satellite remote sensing and ground verification scatter plots. AERONET AOD versus (**a**) AGRI AOD, (**b**) FY4B_LDA AOD, (**c**) AHI AOD, (**d**) MODIS DB AOD, (**e**) MODIS DT AOD at 550 nm. The black dashed lines and red solid lines are the EE lines and regression lines, respectively.

Overall, the AGRI AOD retrievals had higher quality and performed better in China.

4.1.2. Validation in Different Sites

Figure 7 shows the accuracy validation results for the AGRI, FY4B_LDA, AHI, MODIS DB, and DT AOD at different sites. The number of valid matchups was too small (less than 10) due to the low temporal integrity of the AGRI AOD retrievals in QTR, so the validation results for this region were removed to ensure statistical validity. The AGRI AOD retrievals demonstrated high accuracy at most sites in China. More than half of these sites had a correlation coefficient greater than 0.7 and a low RMSE (less than 0.18). The AGRI AOD retrievals had the highest agreement with ground-based measurements in the northern region, with high R values (exceeding 0.8), low RMSE values (less than 0.18), and over 60% of the AOD matchups falling within the EE line. However, the AGRI AOD retrievals were less accurate in the southern region, especially in Taiwan Province, where sites with large errors were found, indicating that the algorithm's applicability in this region needs to be enhanced. The differences in accuracy between sites may be related to inappropriate aerosol modeling. Due to the limited number and uneven distribution of AERONET stations, the applicability of aerosol modeling may vary in different regions, leading to variations in retrieval accuracy. In addition, the representativeness of aerosol models in areas without site distributions warrants further investigation. For example, the Loess Plateau, characterized by a unique topography and geomorphology, may exhibit different aerosol properties compared to other regions in the NR, such as Beijing–Tianjin–Hebei. However, there is no AERONET site in this region, and the aerosol models may differ from the actual aerosol properties, potentially resulting in large biases in retrievals. We will

improve the aerosol modeling method in future studies. The FY4B_LDA AOD product showed high consistency with the ground-based AOD at northern sites, with R values all exceeding 0.7, but low consistency at other sites. In addition, the FY4B_LDA AOD product exhibited a large RMSE (over 0.26) at all sites, indicating a large error. The AHI AOD product exhibited high consistency with the ground-based AOD at most sites, but showed considerable uncertainty in the northern region, with RMSEs exceeding 0.26 and less than 60% of the AOD samples falling within the EE line. The MODIS DB and DT AOD products agreed well with the ground-based AOD at most sites and demonstrated higher accuracy than other products in the southern region. However, for the MODIS DT AOD product, sites with low percentages of AOD samples within the EE envelopes (less than 40%) and high RMSE values (over 0.26) were found in the northern region, indicating large uncertainty in this region.

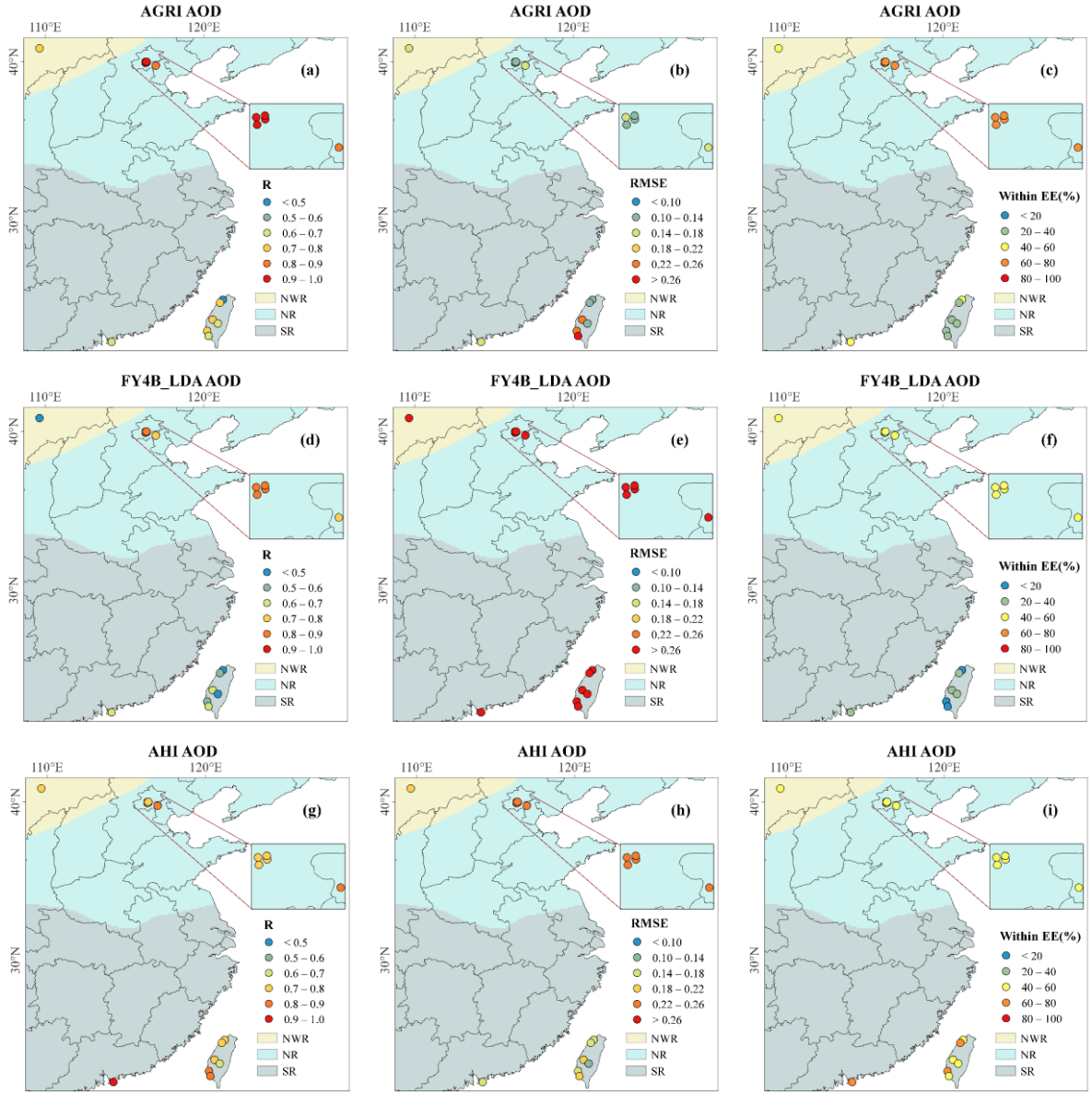


Figure 7. *Cont.*

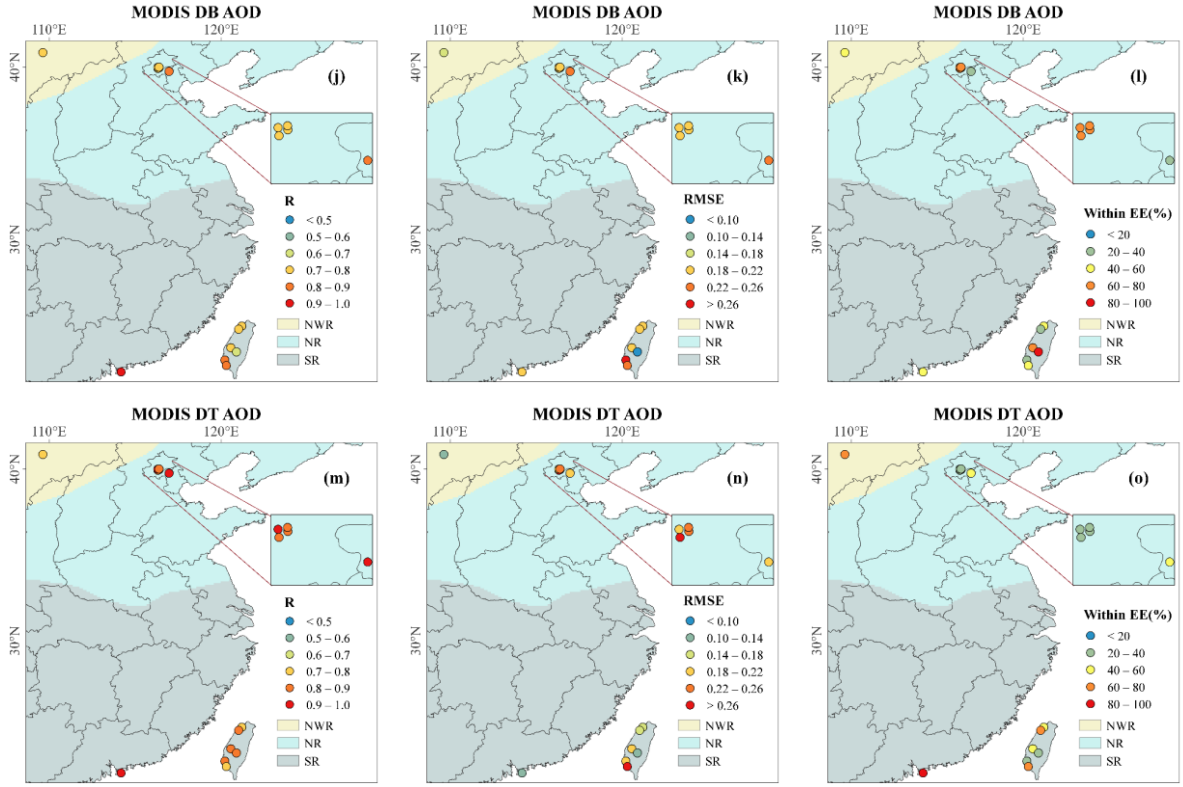


Figure 7. Accuracy evaluation of AGRI, FY4B_LDA, AHI, MODIS DB, and MODIS DT AOD retrievals against ground-based measurements for each site. (**a**,**d**,**g**,**j**,**m**): correlation coefficient (R); (**b**,**e**,**h**,**k**,**n**): root mean square error (RMSE); (**c**,**f**,**i**,**l**,**o**): percentage of AOD within the expected error envelopes (%).

In conclusion, the AGRI AOD retrievals exhibited stable performance with lower uncertainty in most regions of China, especially in the northern region.

4.1.3. Validation in Different Seasons

The evaluation results for different seasons, defined as spring (March, April, and May), summer (June, July, and August), autumn (September, October, and November), and winter (December, January, and February), are shown in Figure 8. As illustrated in the figure, the AGRI AOD retrievals consistently exhibited high accuracy throughout all seasons, with high R values (exceeding 0.8) and low RMSEs (less than 0.18), which was better than FY4B_LDA and AHI AOD, showing the stability of the algorithm. Among them, the AGRI AOD retrievals performed better in autumn and summer, with higher R values (0.91 and 0.89), more matchups within the EE envelopes (67.5% and 79.07%), and low RMSEs (0.14 and 0.11). However, the FY4B_LDA AOD product showed poor accuracy and severe overestimation in all seasons, with high RMSEs (greater than 0.38), RMBs exceeding 1.5, and more than 40% of the samples falling above the EE line. The accuracy of the AHI AOD was lower in autumn and winter, with low correlation coefficient values (R = 0.7) and over 30% of samples above the EE lines, indicating an obvious overestimation. The MODIS DB AOD product demonstrated higher consistency with the ground-based AOD (R = 0.9) in winter and spring, while overestimations and substantial uncertainty existed across all seasons, with high RMBs (over 1.13) and RMSEs (over 0.18). The MODIS DT AOD product agreed well with the ground-based AOD in all seasons, but there were also overestimations, especially in summer, where 69.07% of the samples fell above the EE line. These results indicated that the AGRI AOD retrievals had high accuracy and consistency across all seasons, which demonstrated that the aerosol models for each season were reasonable and the algorithm was applicable in each season.

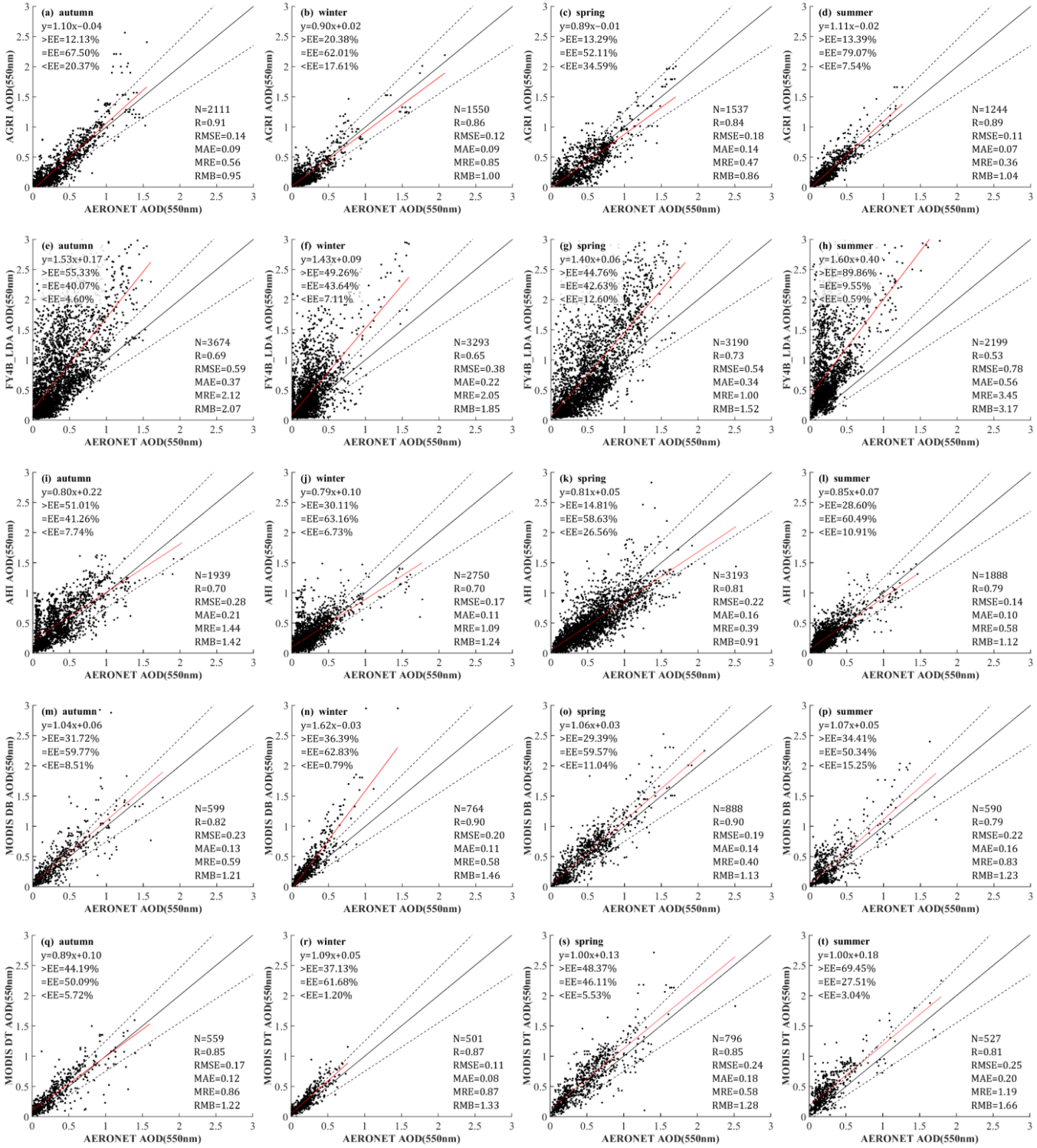


Figure 8. Satellite remote sensing and ground verification scatter plots in different seasons. AERONET AOD versus (**a**–**d**) AGRI AOD, (**e**–**h**) FY4B_LDA AOD, (**i**–**l**) AHI AOD, (**m**–**p**) MODIS DB AOD, (**q**–**t**) MODIS DT AOD at 550 nm.

4.1.4. Validation in Different Months

Different satellite AOD products for each month are validated and compared in this section. As shown in Figure 9, the AGRI AOD retrievals were highly consistent with the ground-based AOD, with R values higher than 0.8, except for January 2023. In addition, the MODIS DB and DT AOD products agreed well with the ground-based AOD, with high R

values (over 0.8) for approximately 83.33% of the months. However, the FY4B_LDA AOD product showed poor agreement with the ground-based AOD, with the lowest R values in most months, while lower R values were found in November and December 2022 for the AHI AOD product.

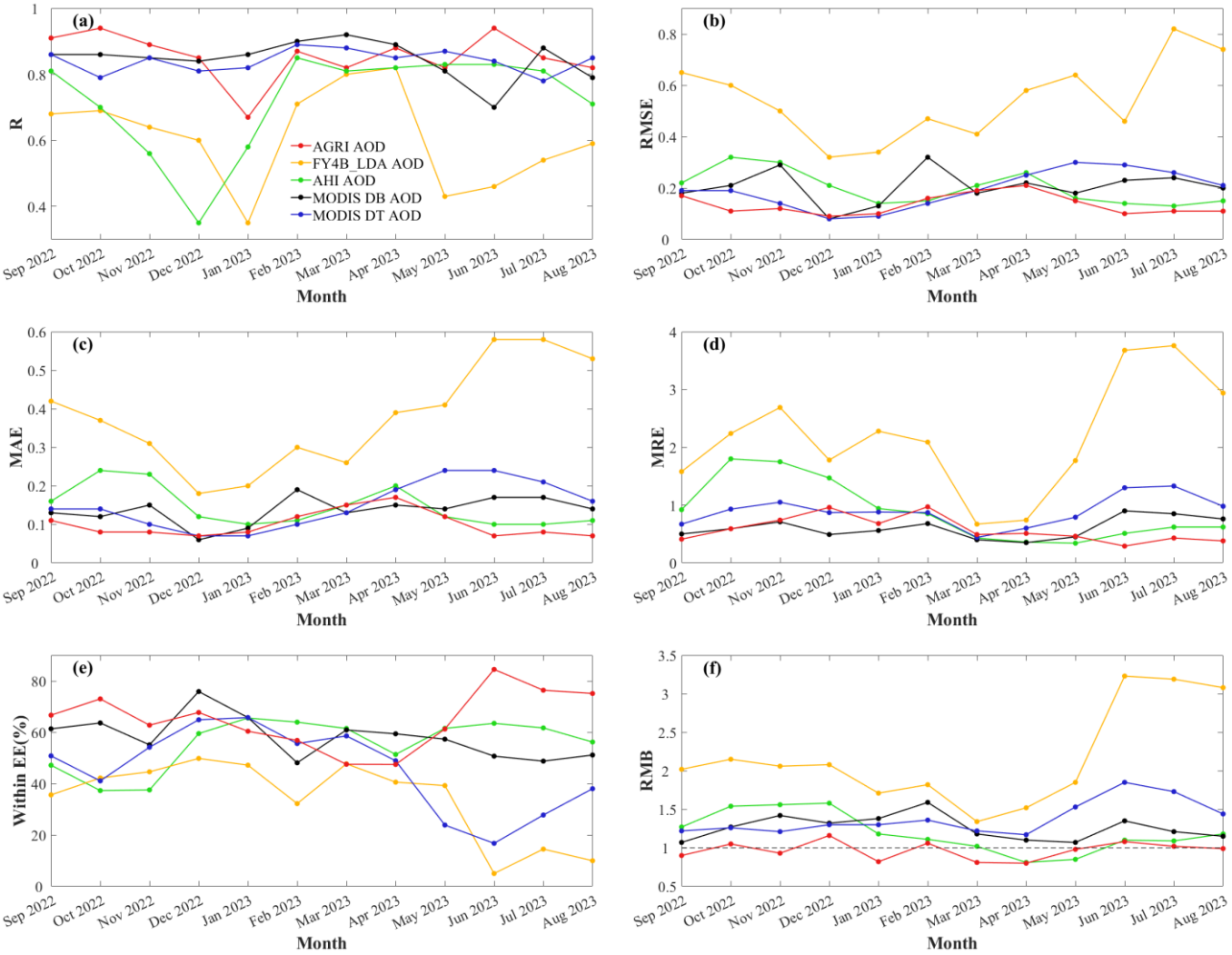


Figure 9. Accuracy evaluation of AGRI, FY4B_LDA, AHI, MODIS DB, and MODIS DT AOD retrievals against ground-based measurements in different months. (**a**): correlation coefficient (R); (**b**): root mean square error (RMSE); (**c**): mean absolute error (MAE); (**d**): mean relative error (MRE); (**e**): percentage of AOD within the expected error envelopes (%); (**f**): relative mean deviation (RMB);.

The AGRI AOD retrievals exhibited small deviations from the ground-based AOD across all months, with RMSE, MAE, and MRE less than 0.25, 0.2, and 1.0, respectively. The MODIS DB AOD product showed large errors in November 2022 and February 2023, while the MODIS DT AOD product showed large errors from May to July 2023. The AHI AOD product had large deviations from September to December 2022, with high RMSEs, MAEs, and MREs. In addition, the FY4B_LDA AOD product had the largest errors across all months, indicating large uncertainties.

As depicted in the Within_EE plot, the percentages of matchups within the EE for the AGRI and MODIS DB AOD retrievals were more than 50% in most months, while the FY4B_LDA AOD product showed low Within_EE values (less than 50%) across all months. In addition, AGRI retrievals had the most AOD matchups that met the EE from September to November 2022 and June to August 2023, indicating better accuracy during these months. The AHI AOD product had lower percentages of matchups within EE from

September to November 2022 compared to other months, while the MODIS DT product showed lower Within_EE values from May to August 2023.

The RMB chart showed that the RMB values for AGRI AOD retrievals were around 1.0 in all months, with the differences from 1.0 being less than 0.2. In contrast, the FY4B_LDA product consistently exhibited significant overestimations across all months, especially from June to August 2023, with RMBs exceeding 3.0. The AHI AOD product showed significant overvaluations from September to December 2022, with the RMB exceeding 1.25, while the RMB values were around 1.0 for the rest of the time. The RMBs for MODIS DB and DT products were greater than 1.0 across all months, with larger RMBs found in February 2023 and from May to August 2023, respectively.

Overall, the AGRI AOD retrievals demonstrated high accuracy and stability across different months and were generally more accurate than other products most of the time.

4.2. Retrieval Error Analysis

To evaluate the AGRI AOD retrievals for different aerosol loadings and properties, an error analysis was performed for the AGRI AOD retrievals. The same assessment was performed for the FY4B_LDA, AHI, MODIS DB, and MODIS DT AOD products for comparison. The AOD matchups were divided into ten bins according to the values of AERONET AOD/AE/SSA, and the median and standard deviation of the bias (i.e., satellite AOD—AERONET AOD) within each bin were calculated separately. Figure 10 shows the dependence of the AOD bias on the AERONET AOD (550 nm), AERONET AE (440–675 nm), and AERONET SSA (440 nm). The result showed that the AGRI AOD retrievals exhibited a positive bias when the aerosol loading was low (AOD < 0.1) and a negative bias when the aerosol loading was moderate (0.1 < AOD < 0.8). The FY4B_LDA AOD product showed a significant positive bias with large standard deviations across all aerosol loadings. The AHI AOD product had a positive bias when AOD < 0.6 and a negative bias when AOD > 0.6. The MODIS DB and DT AOD products showed a positive bias across all aerosol loadings, with the standard deviation of the bias increasing with the AOD value.

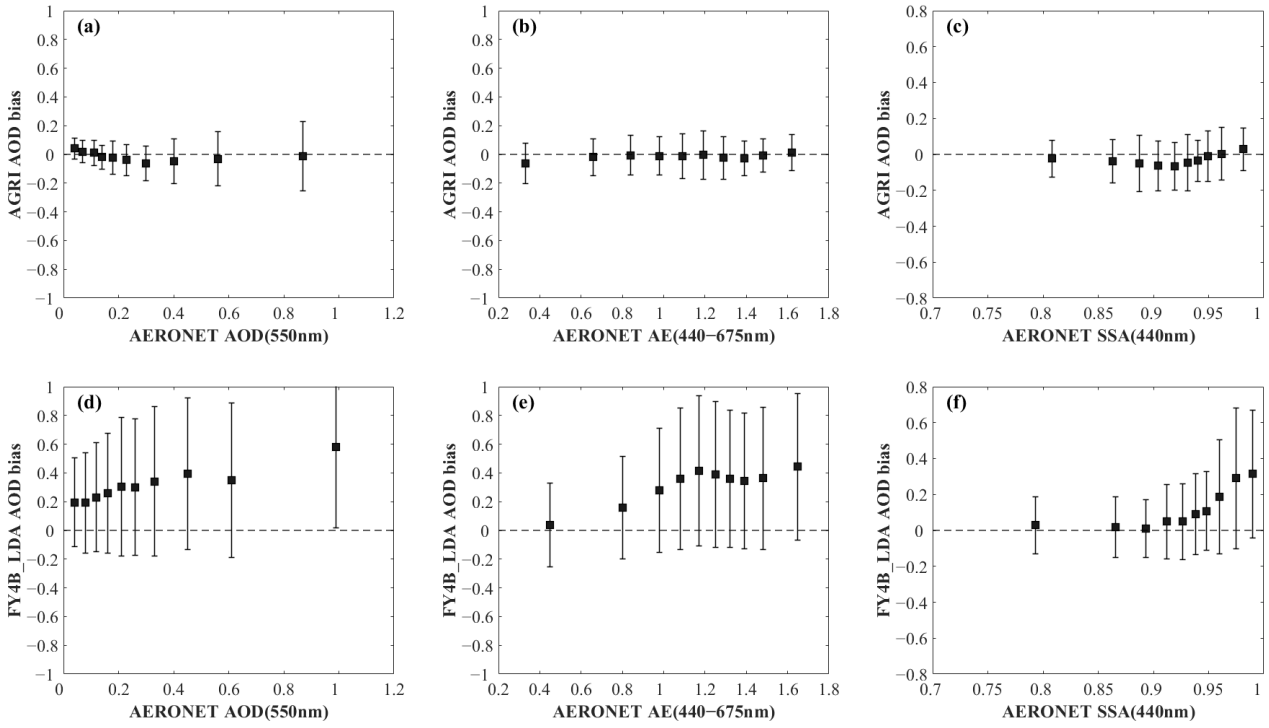


Figure 10. *Cont.*

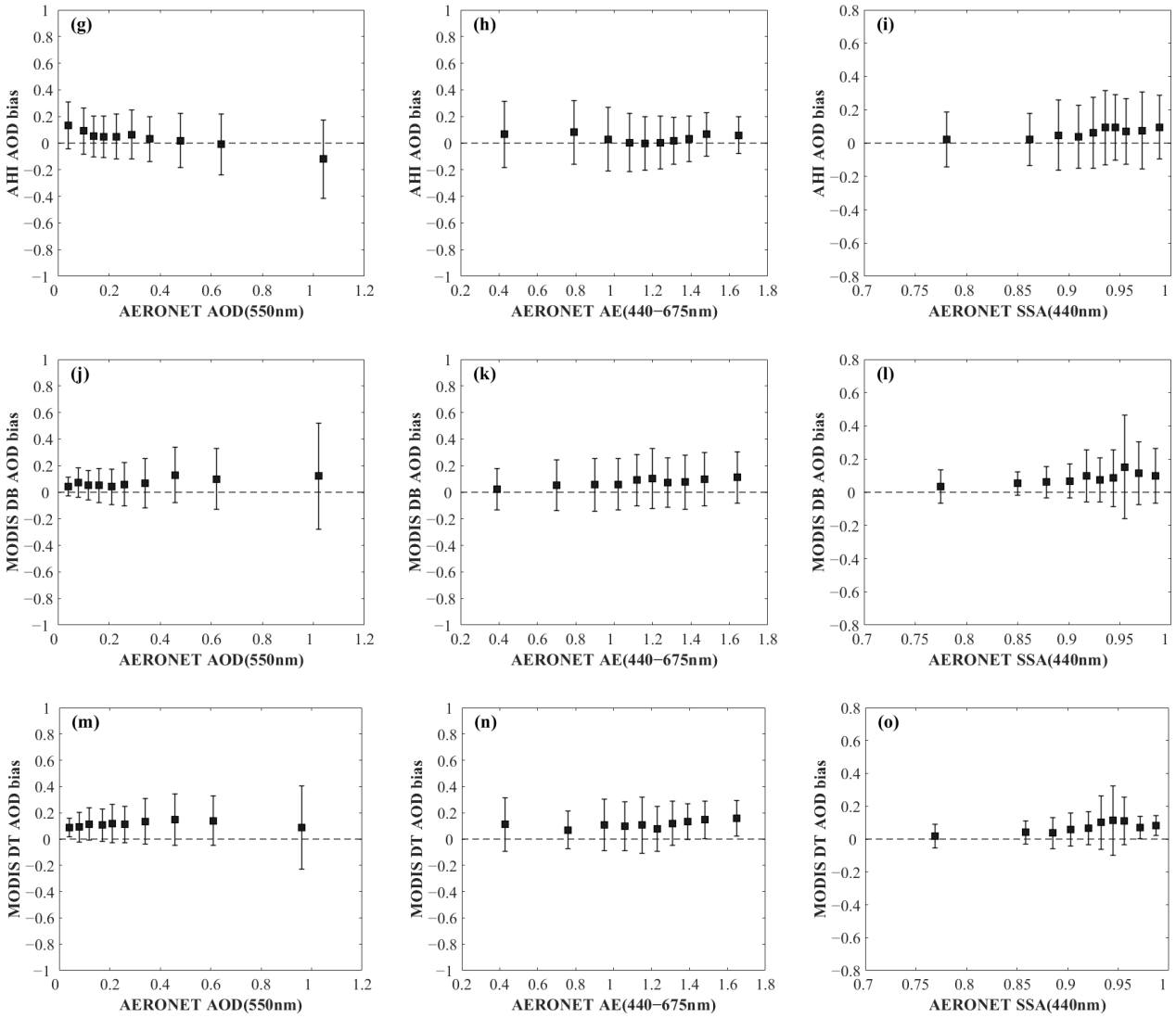


Figure 10. AOD bias (i.e., AGRI AOD—AERONET AOD) in terms of (**a**,**d**,**g**,**j**,**m**) AERONET 550 nm AOD, (**b**,**e**,**h**,**k**,**n**) AERONET 440–675 nm AE, (**c**,**f**,**i**,**l**,**o**) AERONET 440 nm SSA. The black dots and error bars represent the median and standard deviation of the AOD bias.

The AE can be used to represent the size of aerosols, with a smaller AE indicating larger aerosol particles. The median values of the AGRI AOD bias were close to 0 under all AE conditions, except for small AE values (AE < 0.4), where a slight negative deviation was observed, indicating that the AGRI AOD retrievals generally performed well across most aerosol sizes. The FY4B_LDA AOD product exhibited a large positive bias and uncertainty when AE > 0.6, indicating a serious overestimation for small aerosol particles. The AHI AOD product showed no significant bias for medium-sized aerosol particles (1 < AE < 1.4) and displayed a positive bias in other cases. The MODIS DB and DT AOD products exhibited positive biases across all AEs, indicating overestimation. Overall, the AGRI AOD retrievals performed better under various AE conditions with small deviations.

SSA is an important parameter of aerosols, reflecting their absorption characteristics. As shown in Figure 10, when the AERONET SSA was small (SSA < 0.85), the AGRI AOD bias was close to 0 with a small standard deviation, indicating high accuracy for highly absorbent aerosols. AGRI AOD retrievals showed a slight underestimation for aerosols with medium absorption (0.86 < SSA < 0.95). When the SSA was large (SSA > 0.95), the median value of the AGRI AOD bias was close to 0, demonstrating the high accuracy of the retrievals. The FY4B_LDA AOD bias was close to 0 when the SSA was less than

0.89. However, as the SSA increased, the positive bias and the standard deviation of the FY4B_LDA product also increased, showing large uncertainty. The AHI AOD product had a positive bias when SSA > 0.86, indicating an overestimation. The MODIS DB and DT AOD products exhibited a positive bias across all SSA bins, especially when the SSA was around 0.95, where large positive deviations occurred. These results demonstrated the stability of AGRI AOD retrievals for aerosols with different degrees of absorption.

In conclusion, the AGRI AOD retrievals demonstrated high accuracy across various aerosol loadings and properties, demonstrating the stability of the algorithm.

4.3. Spatial Distribution of the Retrieved AOD

Figure 11 shows the spatial distribution of the AGRI AOD retrievals for each hour from 01:00 to 08:00 UTC on 29 September 2022. Figures 12 and 13 display the FY4B_LDA and AHI AOD retrievals for the same time, respectively. The AGRI, FY4B_LDA, and AHI AOD retrievals had similar spatial distribution patterns, with higher aerosol loadings in Northern China, which may be attributed to the population density and high industrial emissions. However, the FY4B_LDA AOD product exhibited abnormally high values in the southern and Tibetan Plateau regions, with no retrieval results in the bright surface areas of the northwest due to algorithmic limitations. In addition, the AGRI AOD exhibited superior spatial integrity compared to the AHI AOD, enabling it to better capture the spatial and temporal variation trends of the AOD within a day. As shown in Figure 11, aerosols were mainly concentrated in the Beijing–Tianjin–Hebei and central regions around 01:00 UTC, gradually spreading northeastward with increasing concentrations over time and peaking around 04:00 UTC. Thereafter, the aerosol concentration and the coverage of high-load aerosols gradually decreased. Figure 14 shows the spatial distribution of the MODIS DB and DT AODs on 29 September 2022, respectively. The spatial distributions of the MOD04 and MYD04 DB AODs were consistent with the AGRI AOD retrievals at 3:00 and 6:00, respectively, while the MODIS DT AODs were largely missing in the western region.

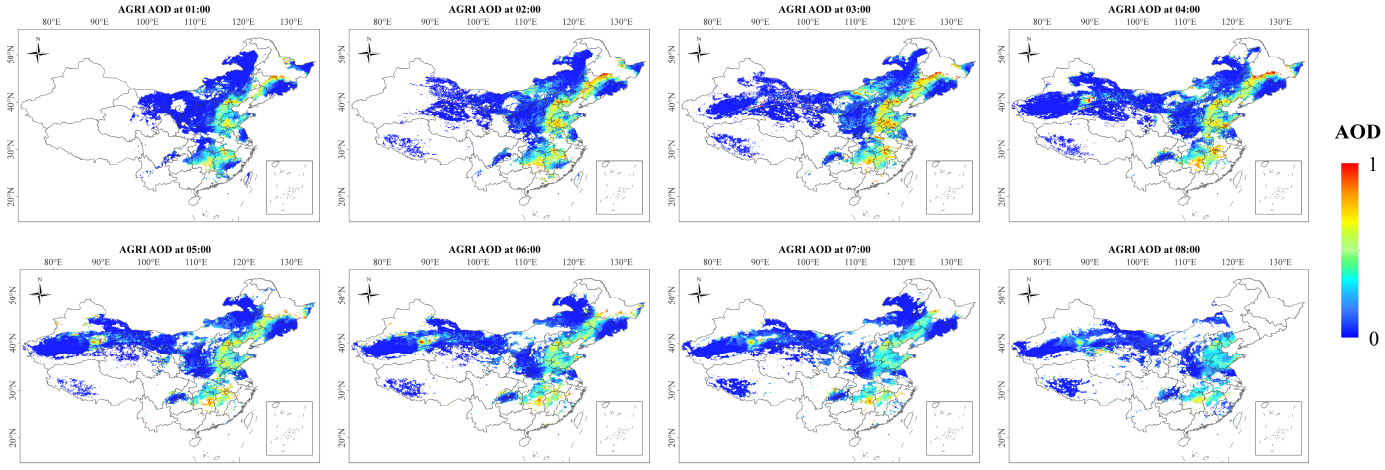


Figure 11. Maps of the AGRI AOD on 29 September 2022, from 01:00 UTC to 08:00 UTC.

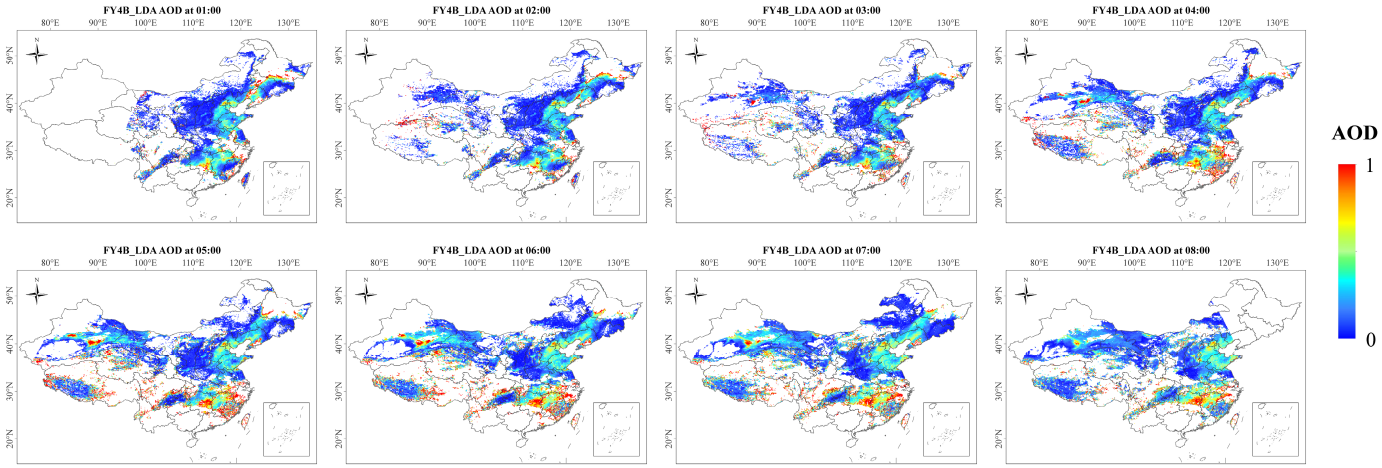


Figure 12. Maps of the FY4B_LDA AOD on 29 September 2022, from 01:00 UTC to 08:00 UTC.

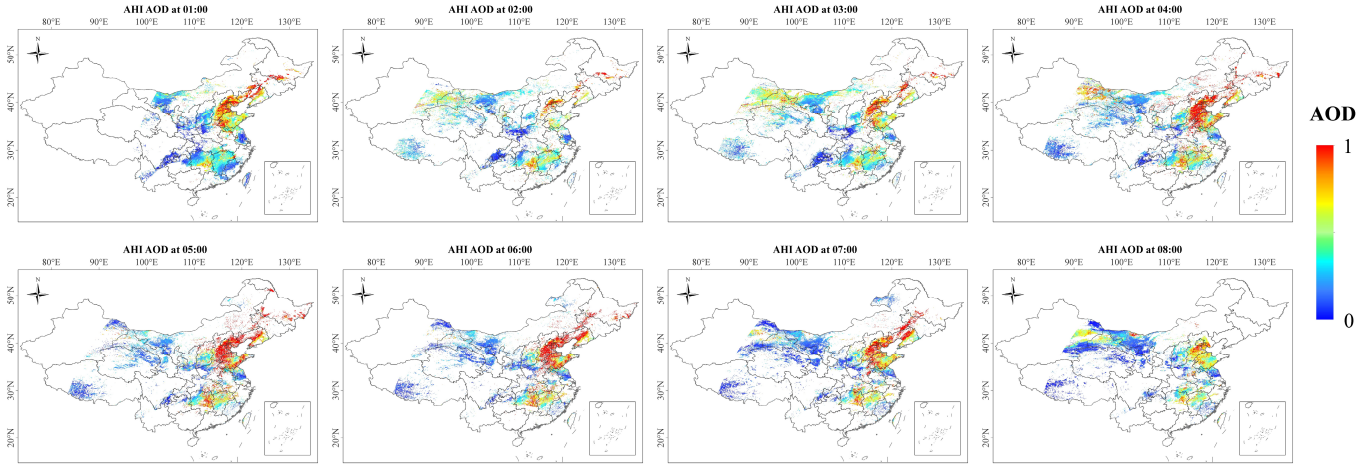


Figure 13. Maps of the AHI AOD on 29 September 2022, from 01:00 UTC to 08:00 UTC.

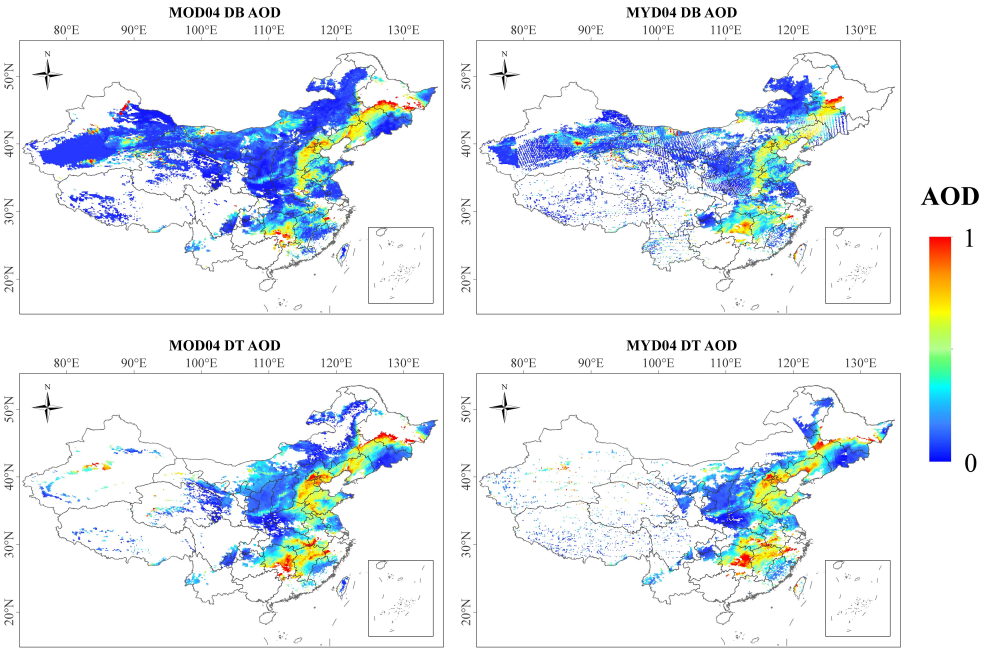


Figure 14. Maps of the MODIS DB AOD and MODIS DT AOD on 29 September 2022.

In summary, the AGRI AOD retrievals demonstrated higher reliability, exhibiting superior spatial integrity compared to the FY4B_LDA and AHI AOD products and a higher temporal resolution than the MODIS AOD products.

Figure 15 shows the spatial distribution of the mean AOD values from AGRI, FY4B_LDA, AHI, and MODIS from September 2022 to August 2023. It can be seen that the AGRI AOD retrievals exhibited a similar spatial pattern to the AHI and MODIS AOD products, with higher AOD values in the North China Plain, Sichuan Basin, and Tarim Basin. However, the AGRI AOD values were comparatively lower than those of the AHI and MODIS AOD products, attributed to the overestimations of the AHI and MODIS AOD products, as well as the slight underestimations of AGRI AOD retrievals. In addition, geostationary satellite AOD averages are more representative of the actual situation due to their higher temporal resolution. However, the FY4B_LDA AOD product exhibited unreasonable overestimations in bright surface areas such as the south, northwest, and Tibetan Plateau, indicating limited applicability in such regions.

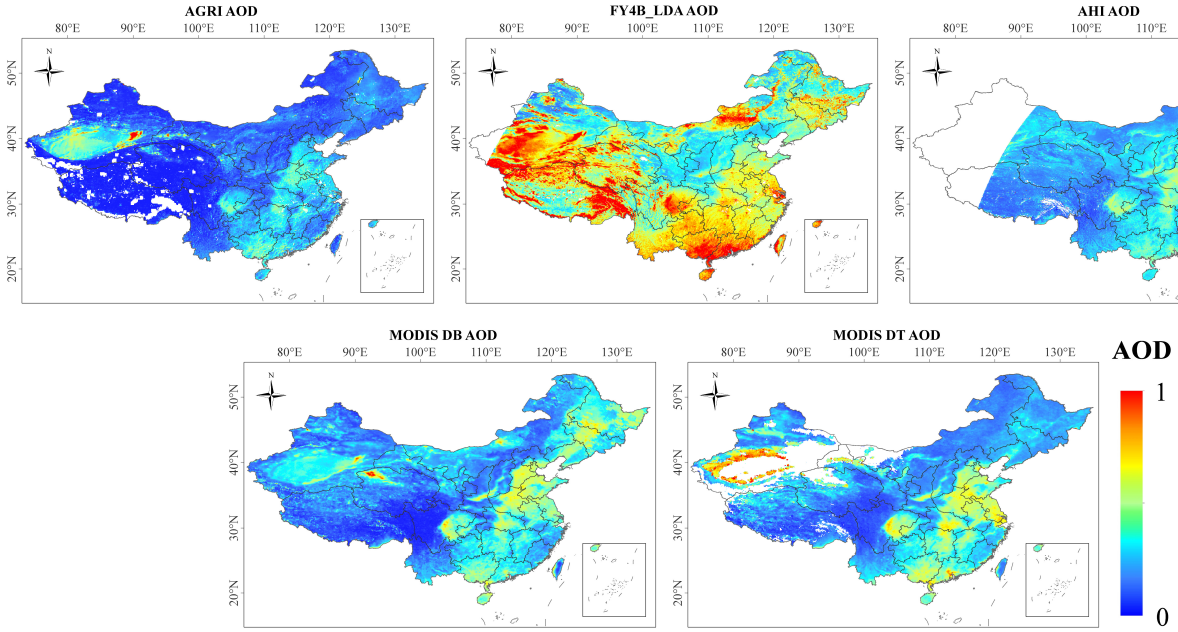


Figure 15. Averaged AOD distributions for AGRI, FY4B_LDA, AHI, MODIS DB, and MODIS DT from September 2022 to August 2023.

In terms of spatial completeness, the AHI AOD product had no data in Northwestern China due to the constraints of the observation conditions. There were few retrievals for "bright targets" in the MODIS DT product, such as the northwestern region, since the DT algorithm is only applicable to dark target areas. In addition, pixels with unreliable negative values were deleted in our algorithm, resulting in fewer AGRI AOD results in the QTR compared to other products. In future studies, we will further improve the AOD retrieval algorithm in the QTR.

In summary, the AGRI AOD retrievals can correctly represent the spatial distribution of the aerosol load, albeit with a slight underestimation. The high temporal integrity and accuracy of AGRI AOD retrievals provide better support for studies on aerosol analysis.

5. Conclusions

High-quality aerosol products play important roles in the study of climate change, human health, and air pollution. The FY-4B is the next-generation geostationary meteorological satellite launched by China, equipped with an AGRI sensor suitable for aerosol retrieval. However, the FY-4B AGRI official AOD product is unsuitable for bright surfaces and exhibits low accuracy. This study proposed an algorithm for AOD retrieval from FY-4B AGRI data that could be applied over the entire land area (except snow/ice and inland

waters). In this method, a monthly BRDF database based on MODIS BRDF products was established as a priori knowledge of surface reflectance. More refined aerosol models depending on the region and season were built based on the AERONET aerosol products in China. The 6SV model was used to build look-up tables of different aerosol models for AOD retrieval. The new method was applied to retrieve the AOD from AGRI measurements in China from September 2022 to August 2023. The retrievals were validated and compared using ground-based measurements and the FY4B_LDA, AHI, MODIS DB, and MODIS DT AOD products.

The overall validation results showed that the AGRI AOD retrievals agreed well with the ground-based measurements (R = 0.88), with a small error (RMSE = 0.14, MAE = 0.1, MRE = 0.57), a high proportion of retrievals meeting quality standards (within EE = 65.04%), and a slight negative bias (RMB = 0.94), making them better than those of the FY4B_LDA, AHI, MODIS DB, and MODIS DT AOD products. Validation across diverse sites demonstrated the robust performance of the AGRI AOD retrievals in most regions of China, with small uncertainty and good agreement with ground-based measurements. Moreover, the AGRI AOD retrievals performed well in different seasons, with R values exceeding 0.84 and RMSEs below 0.18, indicating the algorithm's adaptability in each season. Furthermore, the AGRI AOD retrievals consistently maintained high accuracy over time, showing the algorithm's temporal stability. The error analysis showed the low uncertainty of the AGRI AOD retrievals for most aerosol loadings and properties, demonstrating the robustness of the algorithm. In terms of the spatial distribution of the AOD, AGRI AOD retrievals showed a similar spatial pattern to the MODIS DB AOD product, but with the advantage of a high temporal resolution. This enables AGRI AOD retrievals to capture both the spatial and temporal variations of aerosols over a short period. In summary, the proposed algorithm demonstrates high accuracy and stability. The AGRI AOD retrieved using this algorithm is important for the further exploration of the role of aerosols in climate change and the radiation balance.

Author Contributions: Conceptualization, D.Z., Q.W. and S.L.; methodology, D.Z. and Q.W.; validation, D.Z.; data curation, D.Z. and Q.W.; writing—original draft preparation, D.Z.; writing—review and editing, Q.W., S.L. and J.Y. All authors have read and agreed to the published version of the manuscript.

Funding: This research was funded by the National Natural Science Foundation of China (No. 41975022 and 42205129), the Open Research Program of the International Research Center of Big Data for Sustainable Development Goals (No. CBAS2022ORP01), the China Postdoctoral Science Foundation (No. 2022M712445), and the Wuhan University Specific Fund for Major School-level Internationalization Initiatives.

Data Availability Statement: FY-4B AGRI data for this study are available at (http://satellite.nsmc.org.cn, accessed on 20 November 2023). AHI data for this study are available at (http://www.eorc.jaxa.jp/ptree, accessed on 20 November 2023). MODIS data for this study are available at (http://ladsweb.nascom.nasa.gov, accessed on 20 November 2023). AERONET data for this study are available at (http://aeronet.gsfc.nasa.gov, accessed on 20 November 2023).

Acknowledgments: The authors are grateful to NASA, the National Satellite Meteorological Center, JAXA, and AERONET for the provision of the in situ measurement data and satellite data utilized in this study.

Conflicts of Interest: The authors declare no conflict of interest.

References

1. Zhang, H.; Zhao, S.; Wang, Z.; Zhang, X.; Song, L. The updated effective radiative forcing of major anthropogenic aerosols and their effects on global climate at present and in the future. *Int. J. Climatol.* **2016**, *36*, 4029–4044. [CrossRef]
2. Mahowald, N.; Ward, D.S.; Kloster, S.; Flanner, M.G.; Heald, C.L.; Heavens, N.G.; Hess, P.G.; Lamarque, J.-F.; Chuang, P.Y. Aerosol Impacts on Climate and Biogeochemistry. *Annu. Rev. Environ. Resour.* **2011**, *36*, 45–74. [CrossRef]
3. Scott, C.E.; Arnold, S.R.; Monks, S.A.; Asmi, A.; Paasonen, P.; Spracklen, D.V. Substantial large-scale feedbacks between natural aerosols and climate. *Nat. Geosci.* **2017**, *11*, 44–48. [CrossRef]

4. Colbeck, I.; Lazaridis, M. Aerosols and environmental pollution. *Naturwissenschaften* **2010**, *97*, 117–131. [CrossRef]
5. Chow, J.C.; Watson, J.G.; Mauderly, J.L.; Costa, D.L.; Wyzga, R.E.; Vedal, S.; Hidy, G.M.; Altshuler, S.L.; Marrack, D.; Heuss, J.M.; et al. Health effects of fine particulate air pollution: Lines that connect. *J. Air Waste Manag. Assoc.* **2006**, *56*, 1368–1380. [CrossRef] [PubMed]
6. King, M.D.; Kaufman, Y.J.; Tanre, D.; Nakajima, T. Remote sensing of tropospheric aerosols from space: Past, present, and future. *Bull. Am. Meteorol. Soc.* **1999**, *80*, 2229–2259. [CrossRef]
7. Kaufman, Y.J.; Tanré, D.; Remer, L.A.; Vermote, E.F.; Chu, A.; Holben, B.N. Operational remote sensing of tropospheric aerosol over land from EOS moderate resolution imaging spectroradiometer. *J. Geophys. Res. Atmos.* **1997**, *102*, 17051–17067. [CrossRef]
8. Martonchik, J.V.; Diner, D.J.; Kahn, R.A.; Ackerman, T.P.; Verstraete, M.E.; Pinty, B.; Gordon, H.R. Techniques for the retrieval of aerosol properties over land and ocean using multiangle imaging. *IEEE Trans. Geosci. Remote Sens.* **1998**, *36*, 1212–1227. [CrossRef]
9. Wang, M.H.; Knobelspiesse, K.D.; McClain, C.R. Study of the Sea-Viewing Wide Field-of-View Sensor (SeaWiFS) aerosol optical property data over ocean in combination with the ocean color products. *J. Geophys. Res.-Atmos.* **2005**, *110*, D10S06. [CrossRef]
10. Jackson, J.M.; Liu, H.Q.; Laszlo, I.; Kondragunta, S.; Remer, L.A.; Huang, J.F.; Huang, H.C. Suomi-NPP VIIRS aerosol algorithms and data products. *J. Geophys. Res.-Atmos.* **2013**, *118*, 12673–12689. [CrossRef]
11. Choi, M.; Kim, J.; Lee, J.; Kim, M.; Park, Y.-J.; Holben, B.; Eck, T.F.; Li, Z.; Song, C.H. GOCI Yonsei aerosol retrieval version 2 products: An improved algorithm and error analysis with uncertainty estimation from 5-year validation over East Asia. *Atmos. Meas. Tech.* **2018**, *11*, 385–408. [CrossRef]
12. She, L.; Xue, Y.; Yang, X.; Leys, J.; Guang, J.; Che, Y.; Fan, C.; Xie, Y.; Li, Y. Joint Retrieval of Aerosol Optical Depth and Surface Reflectance Over Land Using Geostationary Satellite Data. *IEEE Trans. Geosci. Remote Sens.* **2019**, *57*, 1489–1501. [CrossRef]
13. Su, X.; Wang, L.; Zhang, M.; Qin, W.; Bilal, M. A High-Precision Aerosol Retrieval Algorithm (HiPARA) for Advanced Himawari Imager (AHI) data: Development and verification. *Remote Sens. Environ.* **2021**, *253*, 112221. [CrossRef]
14. Levy, R.C.; Remer, L.A.; Dubovik, O. Global aerosol optical properties and application to Moderate Resolution Imaging Spectroradiometer aerosol retrieval over land. *J. Geophys. Res. Atmos.* **2007**, *112*, D13210. [CrossRef]
15. Levy, R.C.; Remer, L.A.; Mattoo, S.; Vermote, E.F.; Kaufman, Y.J. Second-generation operational algorithm: Retrieval of aerosol properties over land from inversion of Moderate Resolution Imaging Spectroradiometer spectral reflectance. *J. Geophys. Res. Atmos.* **2007**, *112*, D13211. [CrossRef]
16. Levy, R.C.; Mattoo, S.; Munchak, L.A.; Remer, L.A.; Sayer, A.M.; Patadia, F.; Hsu, N.C. The Collection 6 MODIS aerosol products over land and ocean. *Atmos. Meas. Tech.* **2013**, *6*, 2989–3034. [CrossRef]
17. Hsu, N.C.; Tsay, S.C.; King, M.D.; Herman, J.R. Deep Blue Retrievals of Asian Aerosol Properties During ACE-Asia. *IEEE Trans. Geosci. Remote Sens.* **2006**, *44*, 3180–3195. [CrossRef]
18. Hsu, N.C.; Jeong, M.J.; Bettenhausen, C.; Sayer, A.M.; Hansell, R.; Seftor, C.S.; Huang, J.; Tsay, S.C. Enhanced Deep Blue aerosol retrieval algorithm: The second generation. *J. Geophys. Res. Atmos.* **2013**, *118*, 9296–9315. [CrossRef]
19. Lyapustin, A.; Wang, Y.; Laszlo, I.; Kahn, R.; Korkin, S.; Remer, L.; Levy, R.; Reid, J.S. Multiangle implementation of atmospheric correction (MAIAC): 2. Aerosol algorithm. *J. Geophys. Res.* **2011**, *116*, D03211. [CrossRef]
20. Kim, M.; Kim, J.; Wong, M.S.; Yoon, J.; Lee, J.; Wu, D.; Chan, P.W.; Nichol, J.E.; Chung, C.-Y.; Ou, M.-L. Improvement of aerosol optical depth retrieval over Hong Kong from a geostationary meteorological satellite using critical reflectance with background optical depth correction. *Remote Sens. Environ.* **2014**, *142*, 176–187. [CrossRef]
21. Lim, H.; Choi, M.; Kim, J.; Kasai, Y.; Chan, P. AHI/Himawari-8 Yonsei Aerosol Retrieval (YAER): Algorithm, Validation and Merged Products. *Remote Sens.* **2018**, *10*, 699. [CrossRef]
22. Yoshida, M.; Kikuchi, M.; Nagao, T.M.; Murakami, H.; Nomaki, T.; Higurashi, A. Common Retrieval of Aerosol Properties for Imaging Satellite Sensors. *J. Meteorol. Soc. Jpn. Ser. II* **2018**, *96B*, 193–209. [CrossRef]
23. Ge, B.; Li, Z.; Liu, L.; Yang, L.; Chen, X.; Hou, W.; Zhang, Y.; Li, D.; Li, L.; Qie, L. A Dark Target Method for Himawari-8/AHI Aerosol Retrieval: Application and Validation. *IEEE Trans. Geosci. Remote Sens.* **2019**, *57*, 381–394. [CrossRef]
24. Gupta, P.; Levy, R.C.; Mattoo, S.; Remer, L.A.; Holz, R.E.; Heidinger, A.K. Applying the Dark Target aerosol algorithm with Advanced Himawari Imager observations during the KORUS-AQ field campaign. *Atmos. Meas. Tech.* **2019**, *12*, 6557–6577. [CrossRef]
25. Wang, Q.; Li, S.; Zeng, Q.; Sun, L.; Yang, J.; Lin, H. Retrieval and Validation of AOD from Himawari-8 Data over Bohai Rim Region, China. *Remote Sens.* **2020**, *12*, 3425. [CrossRef]
26. Zhang, Z.; Fan, M.; Wu, W.; Wang, Z.; Tao, M.; Wei, J.; Wang, Q. A simplified aerosol retrieval algorithm for Himawari-8 Advanced Himawari Imager over Beijing. *Atmos. Environ.* **2019**, *199*, 127–135. [CrossRef]
27. Wang, Q.; Du, D.; Li, S.; Yang, J.; Lin, H.; Du, J. Comparison of different methods of determining land surface reflectance for AOD retrieval. *Atmos. Pollut. Res.* **2021**, *12*, 101143. [CrossRef]
28. Yang, J.; Zhang, Z.Q.; Wei, C.Y.; Lu, F.; Guo, Q. INTRODUCING THE NEW GENERATION OF CHINESE GEOSTATIONARY WEATHER SATELLITES, FENGYUN-4. *Bull. Am. Meteorol. Soc.* **2017**, *98*, 1637–1658. [CrossRef]
29. Xie, Y.; Li, Z.; Guang, J.; Hou, W.; Salam, A.; Ali, Z.; Fang, L. Aerosol Optical Depth Retrieval Over South Asia Using FY-4A/AGRI Data. *IEEE Trans. Geosci. Remote Sens.* **2022**, *60*, 4104814. [CrossRef]
30. Jiang, X.; Xue, Y.; Jin, C.; Bai, R.; Sun, Y.; Wu, S. A Simple Band Ratio Library (BRL) Algorithm for Retrieval of Hourly Aerosol Optical Depth Using FY-4A AGRI Geostationary Satellite Data. *Remote Sens.* **2022**, *14*, 4861. [CrossRef]

31. Lyapustin, A.; Wang, Y.; Korkin, S.; Huang, D. MODIS Collection 6 MAIAC algorithm. *Atmos. Meas. Tech.* **2018**, *11*, 5741–5765. [CrossRef]
32. Bessho, K.; Date, K.; Hayashi, M.; Ikeda, A.; Imai, T.; Inoue, H.; Kumagai, Y.; Miyakawa, T.; Murata, H.; Ohno, T.; et al. An Introduction to Himawari-8/9-Japan's New-Generation Geostationary Meteorological Satellites. *J. Meteorol. Soc. Jpn.* **2016**, *94*, 151–183. [CrossRef]
33. Holben, B.N.; Eck, T.F.; Slutsker, I.; Tanre, D.; Buis, J.P.; Setzer, A.; Vermote, E.; Reagan, J.A.; Kaufman, Y.J.; Nakajima, T.; et al. AERONET—A federated instrument network and data archive for aerosol characterization. *Remote Sens. Environ.* **1998**, *66*, 1–16. [CrossRef]
34. Remer, L.A.; Kaufman, Y.J.; Tanre, D.; Mattoo, S.; Chu, D.A.; Martins, J.V.; Li, R.R.; Ichoku, C.; Levy, R.C.; Kleidman, R.G.; et al. The MODIS aerosol algorithm, products, and validation. *J. Atmos. Sci.* **2005**, *62*, 947–973. [CrossRef]
35. Sayer, A.M.; Hsu, N.C.; Bettenhausen, C.; Jeong, M.J. Validation and uncertainty estimates for MODIS Collection 6 "Deep Blue" aerosol data. *J. Geophys. Res.-Atmos.* **2013**, *118*, 7864–7872. [CrossRef]
36. Dubovik, O.; King, M.D. A flexible inversion algorithm for retrieval of aerosol optical properties from Sun and sky radiance measurements. *J. Geophys. Res.-Atmos.* **2000**, *105*, 20673–20696. [CrossRef]
37. Zhang, L.; Li, J. Variability of Major Aerosol Types in China Classified Using AERONET Measurements. *Remote Sens.* **2019**, *11*, 2334. [CrossRef]
38. Sinyuk, A.; Holben, B.N.; Eck, T.F.; Giles, D.M.; Slutsker, I.; Korkin, S.; Schafer, J.S.; Smirnov, A.; Sorokin, M.; Lyapustin, A. The AERONET Version 3 aerosol retrieval algorithm, associated uncertainties and comparisons to Version 2. *Atmos. Meas. Tech.* **2020**, *13*, 3375–3411. [CrossRef]
39. Wang, Q.; Li, S.; Yang, J.; Zhou, D. Evaluation and comparison of VIIRS dark target and deep blue aerosol products over land. *Sci. Total Environ.* **2023**, *869*, 161667. [CrossRef]
40. Giles, D.M.; Sinyuk, A.; Sorokin, M.G.; Schafer, J.S.; Smirnov, A.; Slutsker, I.; Eck, T.F.; Holben, B.N.; Lewis, J.R.; Campbell, J.R.; et al. Advancements in the Aerosol Robotic Network (AERONET) Version 3 database–automated near-real-time quality control algorithm with improved cloud screening for Sun photometer aerosol optical depth (AOD) measurements. *Atmos. Meas. Tech.* **2019**, *12*, 169–209. [CrossRef]
41. Wang, Y.; Chen, L.F.; Li, S.S.; Wang, X.H.; Yu, C.; Si, Y.D.; Zhang, Z.L. Interference of Heavy Aerosol Loading on the VIIRS Aerosol Optical Depth (AOD) Retrieval Algorithm. *Remote Sens.* **2017**, *9*, 397. [CrossRef]
42. Wang, Q.; Li, S.; Yang, J.; Zhou, D.; Song, G. A high-precision aerosol retrieval algorithm for FY-3D MERSI-II images. *Environ. Int.* **2023**, *173*, 107841. [CrossRef]
43. Kim, D.-H. Aerosol optical properties over east Asia determined from ground-based sky radiation measurements. *J. Geophys. Res.* **2004**, *109*, D02209. [CrossRef]
44. He, Q.Q.; Gu, Y.F.; Zhang, M. Spatiotemporal patterns of aerosol optical depth throughout China from 2003 to 2016. *Sci. Total Environ.* **2019**, *653*, 23–35. [CrossRef]
45. Wei, J.; Li, Z.; Peng, Y.; Sun, L.; Yan, X. A Regionally Robust High-Spatial-Resolution Aerosol Retrieval Algorithm for MODIS Images Over Eastern China. *IEEE Trans. Geosci. Remote Sens.* **2019**, *57*, 4748–4757. [CrossRef]
46. Chen, Q.-X.; Huang, C.-L.; Yuan, Y.; Mao, Q.-J.; Tan, H.-P. Spatiotemporal Distribution of Major Aerosol Types over China Based on MODIS Products between 2008 and 2017. *Atmosphere* **2020**, *11*, 703. [CrossRef]
47. Hayasaka, T.; Luo, Y.; Zheng, X.; Zhao, T.; Luo, H.; Nakamura, K.; Im, E. Geographical and climatological characterization of aerosol optical depth distribution of MODIS in China. In Proceedings of the SPIE Asia-Pacific Remote Sensing, Kyoto, Japan, 29 October–1 November 2012; Volume 8523, p. 85231N. [CrossRef]
48. Filonchyk, M.; Yan, H.; Zhang, Z. Analysis of spatial and temporal variability of aerosol optical depth over China using MODIS combined Dark Target and Deep Blue product. *Theor. Appl. Climatol.* **2018**, *137*, 2271–2288. [CrossRef]
49. Yang, X.; Zhao, C.; Zhou, L.; Wang, Y.; Liu, X. Distinct impact of different types of aerosols on surface solar radiation in China. *J. Geophys. Res. Atmos.* **2016**, *121*, 6459–6471. [CrossRef]
50. Su, X.; Goloub, P.; Chiapello, I.; Chen, H.; Ducos, F.; Li, Z. Aerosol variability over East Asia as seen by POLDER space-borne sensors. *J. Geophys. Res. Atmos.* **2010**, *115*, D24215. [CrossRef]
51. Cheng, L.; Li, L.; Chen, L.; Hu, S.; Yuan, L.; Liu, Y.; Cui, Y.; Zhang, T. Spatiotemporal Variability and Influencing Factors of Aerosol Optical Depth over the Pan Yangtze River Delta during the 2014–2017 Period. *Int. J. Environ. Res. Public Health* **2019**, *16*, 3522. [CrossRef]
52. Yuan, T.G.; Chen, S.Y.; Huang, J.P.; Wu, D.Y.; Lu, H.; Zhang, G.L.; Ma, X.J.; Chen, Z.Q.; Luo, Y.; Ma, X.H. Influence of Dynamic and Thermal Forcing on the Meridional Transport of Taklimakan Desert Dust in Spring and Summer. *J. Clim.* **2019**, *32*, 749–767. [CrossRef]
53. Han, Y.; Wang, T.H.; Tang, J.Y.; Wang, C.Y.; Jian, B.D.; Huang, Z.W.; Huang, J.P. New insights into the Asian dust cycle derived from CALIPSO lidar measurements. *Remote Sens. Environ.* **2022**, *272*, 112906. [CrossRef]
54. Fukuda, S.; Nakajima, T.; Takenaka, H.; Higurashi, A.; Kikuchi, N.; Nakajima, T.Y.; Ishida, H. New approaches to removing cloud shadows and evaluating the 380 nm surface reflectance for improved aerosol optical thickness retrievals from the GOSAT/TANSO-Cloud and Aerosol Imager. *J. Geophys. Res.-Atmos.* **2013**, *118*, 13520–13531. [CrossRef]

55. Mei, L.; Zhao, C.; de Leeuw, G.; Che, H.; Che, Y.; Rozanov, V.; Vountas, M.; Burrows, J.P. Understanding MODIS dark-target collection 5 and 6 aerosol data over China: Effect of surface type, aerosol loading and aerosol absorption. *Atmos. Res.* **2019**, *228*, 161–175. [CrossRef]
56. Wei, J.; Sun, L. Comparison and Evaluation of Different MODIS Aerosol Optical Depth Products Over the Beijing-Tianjin-Hebei Region in China. *IEEE J. Sel. Top. Appl. Earth Obs. Remote Sens.* **2017**, *10*, 835–844. [CrossRef]
57. Wei, J.; Li, Z.; Sun, L.; Peng, Y.; Zhang, Z.; Li, Z.; Su, T.; Feng, L.; Cai, Z.; Wu, H. Evaluation and uncertainty estimate of next-generation geostationary meteorological Himawari-8/AHI aerosol products. *Sci. Total Environ.* **2019**, *692*, 879–891. [CrossRef]

Disclaimer/Publisher's Note: The statements, opinions and data contained in all publications are solely those of the individual author(s) and contributor(s) and not of MDPI and/or the editor(s). MDPI and/or the editor(s) disclaim responsibility for any injury to people or property resulting from any ideas, methods, instructions or products referred to in the content.